



**HAL**  
open science

## **Inherited deficiency of stress granule ZNFX1 in patients with monocytosis and mycobacterial disease**

Tom Le Voyer, Anna-Lena Neehus, Rui Yang, Masato Ogishi, Jérémie Rosain, Fayhan Alroqi, Maha Alshalan, Sophie Blumental, Fatima Al Ali, Taushif Khan, et al.

### ► **To cite this version:**

Tom Le Voyer, Anna-Lena Neehus, Rui Yang, Masato Ogishi, Jérémie Rosain, et al.. Inherited deficiency of stress granule ZNFX1 in patients with monocytosis and mycobacterial disease. *Proceedings of the National Academy of Sciences of the United States of America*, 2021, 118 (15), pp.e2102804118. 10.1073/pnas.2102804118 . hal-03371686

**HAL Id: hal-03371686**

**<https://hal.science/hal-03371686v1>**

Submitted on 12 Oct 2021

**HAL** is a multi-disciplinary open access archive for the deposit and dissemination of scientific research documents, whether they are published or not. The documents may come from teaching and research institutions in France or abroad, or from public or private research centers.

L'archive ouverte pluridisciplinaire **HAL**, est destinée au dépôt et à la diffusion de documents scientifiques de niveau recherche, publiés ou non, émanant des établissements d'enseignement et de recherche français ou étrangers, des laboratoires publics ou privés.

## **Inherited deficiency of stress granule-associated ZNFX1 in patients with monocytosis and mycobacterial disease**

Tom Le Voyer<sup>a,b</sup>, Anna-Lena Neehus<sup>a,b,1</sup>, Rui Yang<sup>c,1</sup>, Jérémie Rosain<sup>a,b,1</sup>, Masato Ogishi<sup>c,1</sup>, Fayhan Alroqi<sup>d,e</sup>, Maha Alshalan<sup>f</sup>, Sophie Blumental<sup>g</sup>, Fatima Al Ali<sup>h</sup>, Taushif Khan<sup>h</sup>, Manar Ata<sup>h</sup>, Laurence Rozen<sup>i</sup>, Anne Demulder<sup>i</sup>, Paul Bastard<sup>a,b</sup>, Conor Gruber<sup>j,k,1</sup>, Manon Roynard<sup>a,b</sup>, Yoann Seeleuthener<sup>a,b</sup>, Franck Rapaport<sup>c</sup>, Benedetta Bigio<sup>c</sup>, Maya Chrabieh<sup>a,b</sup>, Danielle Sng<sup>m</sup>, Laureline Berteloot<sup>n</sup>, Nathalie Boddaert<sup>b,n</sup>, Flore Rozenberg<sup>o</sup>, Saleh Al-Muhsen<sup>p</sup>, Aida Bertoli-Avella<sup>q</sup>, Laurent Abel<sup>a,b,c</sup>, Dusan Bogunovic<sup>i,j,k</sup>, Nico Marr<sup>h,r</sup>, Davood Mansouri<sup>s,t</sup>, Fuad Al Mutairi<sup>e,f,2</sup>, Vivien Béziat<sup>a,b,c,2</sup>, Dominique Weil<sup>u,2</sup>, Seyed Alireza Mahdaviani<sup>s,2</sup>, Alina Ferster<sup>v,2</sup>, Shen-Ying Zhang<sup>a,b,c,2</sup>, Bruno Reversade<sup>m,2</sup>, Stéphanie Boisson-Dupuis<sup>a,b,c,2</sup>, Jean-Laurent Casanova<sup>a,b,c,w,3,@</sup>, Jacinta Bustamante<sup>a,b,c,x,3,@</sup>

<sup>a</sup> Laboratory of Human Genetics of Infectious Diseases, Necker Branch, INSERM UMR1163, 75015 Paris, France, EU

<sup>b</sup> University of Paris, Imagine Institute, 75015 Paris, France, EU

<sup>c</sup> St. Giles Laboratory of Human Genetics of Infectious Diseases, Rockefeller Branch, the Rockefeller University, New York, NY 10065, USA

<sup>d</sup> Immunology Division, Department of Pediatrics, King Abdulaziz Medical City, Riyadh 11426, Saudi Arabia.

<sup>e</sup> King Abdullah International Medical Research Center (KAIMRC), King Saud Bin Abdulaziz University for Health Sciences, Riyadh 11426, Saudi Arabia

<sup>f</sup> Genetics & Precision Medicine Department, King Abdullah specialized Children's Hospital, King Abdulaziz Medical City, Riyadh 11426, Saudi Arabia

<sup>g</sup> Paediatric Infectious Diseases Unit, Queen Fabiola Children's University Hospital, 1020 Brussels, Belgium, EU

<sup>h</sup> Research Branch, Sidra Medicine, Doha, Qatar

<sup>i</sup> Laboratory of Hematology LHUB-ULB, Université Libre de Bruxelles ULB, 1020 Brussels, Belgium, EU

<sup>j</sup> Department of Microbiology, Icahn School of Medicine at Mount Sinai, NY 10029, USA

<sup>k</sup> Department of Pediatrics, Icahn School of Medicine at Mount Sinai, NY 10029, USA

<sup>l</sup> The Mindich Child Health and Development Institute, Icahn School of Medicine at Mount Sinai, NY 10029, USA

<sup>m</sup> Laboratory of Human and Therapeutics, Genome Institute of Singapore, A\*STAR 138648 Singapore

<sup>n</sup> Pediatric Radiology Department, AP-HP, Necker Hospital for Sick Children, 75015 Paris, France, EU

<sup>o</sup> Virology Laboratory, Cochin Hospital, University of Paris, 75014 Paris, France, EU

<sup>p</sup> Immunology Research Laboratory, College of Medicine, King Saud University, Riyadh 114362, Saudi Arabia

<sup>q</sup> Department of Genomic Research, CENTOGENE GmbH, 18055, Rostock, Germany, EU

<sup>r</sup> College of Health and Life Sciences, Hamad Bin Khalifa University, Doha, Qatar

<sup>s</sup> Pediatric Respiratory Diseases Research Center, National Research Institute of Tuberculosis and Lung Diseases (NRITLD), Shahid Beheshti University of Medical Sciences, Tehran, Iran

<sup>t</sup> Department of Clinical Immunology and Infectious Diseases, National Research Institute of Tuberculosis and Lung Diseases, Shahid Beheshti University of Medical Sciences, Tehran 19569-44413, Iran

<sup>u</sup> Sorbonne University, CNRS, Paris-Seine Biology Institute (IBPS), Laboratory of Biology of Development, 75005, Paris, France, EU

<sup>v</sup> Hemato-oncology Unit, Queen Fabiola Children's University Hospital, Brussels, 1020 Belgium, EU

<sup>w</sup> Howard Hughes Medical Institute, New York, NY 10065, USA

<sup>x</sup> Study Center of Immunodeficiencies, Necker Hospital for Sick Children, 75015 Paris, France, EU

<sup>1,2,3</sup> equal contributions

@ casanova@rockefeller.edu, [jacinta.bustamante@inserm.fr](mailto:jacinta.bustamante@inserm.fr)

**Key words:** mycobacteria, monocytosis, inflammation, inborn error of immunity, ZNFX1

#### **Disclosure of Conflicts of Interest**

The authors have no conflict of interest to declare.

## Abstract

Human inborn errors of IFN- $\gamma$  underlie mycobacterial disease, due to insufficient IFN- $\gamma$  production by lymphoid cells, impaired myeloid cell responses to this cytokine, or both. We report four patients from two unrelated kindreds with intermittent monocytosis and mycobacterial disease, including BCG-osis and disseminated tuberculosis, and without any known inborn error of IFN- $\gamma$ . The patients are homozygous for *ZNFX1* variants (p.S959\* and p.E1606Rfs\*10) predicted to be loss-of-function (pLOF). There are no subjects homozygous for pLOF variants in public databases. *ZNFX1* is a conserved and broadly expressed helicase, but its biology remains largely unknown. It is thought to act as a viral dsRNA sensor in mice, but these patients do not suffer from severe viral illnesses. We analyze its sub-cellular localization upon over-expression in A549 and HeLa cell lines and upon stimulation of THP1 and fibroblastic cell lines. We find that this protein is cytoplasmic and colocalizes with ribonucleoprotein granules called stress granules. The endogenous *ZNFX1* protein in cell lines of the patient homozygous for the p.E1606Rfs\*10 variant is truncated, whereas *ZNFX1* expression is abolished in cell lines from the patients with the p.S959\* variant. Lymphocyte subsets are present at normal frequencies in these patients and produce IFN- $\gamma$  normally. The hematopoietic and non-hematopoietic cells of the patients tested respond normally to IFN- $\gamma$ . Our results indicate that human *ZNFX1* has RNA-binding activity in stress granules and that it is essential for monocyte homeostasis and protective immunity to mycobacteria.

### **Significance statement**

Mendelian susceptibility to mycobacterial disease (MSMD) is defined by selective vulnerability to weakly virulent mycobacteria. The 32 known inborn errors of IFN- $\gamma$  immunity account for MSMD in about half the patients, and for a smaller proportion of cases of tuberculosis (TB). We report homozygous *ZNFX1* variants in two families in which the index cases had MSMD or TB with intermittent monocytosis. Upon overexpression, the two variants encode truncated proteins. We show that human ZNFX1 is localized in ribonucleoprotein granules called stress granules. The patients' production of and response to IFN- $\gamma$  are apparently intact, and the patients have not experienced severe viral illnesses. Inherited deficiency of stress granule associated-ZNFX1 is a genetic etiology of MSMD or TB with intermittent monocytosis.

## Introduction

Mycobacteria cause three major endemic illnesses — tuberculosis (TB), leprosy, and Buruli ulcer — and rarer illnesses caused by less virulent live bacillus Calmette-Guérin (BCG) vaccines or ‘atypical’ environmental mycobacteria. Rare patients with a selective predisposition to clinical disease caused by BCG vaccine and environmental mycobacteria (EM) have Mendelian susceptibility to mycobacterial disease (MSMD) (1, 2). These patients are also prone to disease caused by the more virulent *Mycobacterium tuberculosis*, and intramacrophagic pathogens, such as *Salmonella* species. Their mycobacterial infections range from acute to recurrent or chronic, with localized to regional or disseminated clinical manifestations. Germline mutations of 17 genes (*CYBB*, *IFNG*, *IFNGR1*, *IFNGR2*, *IL12B*, *IL12RB1*, *IL12RB2*, *IL23R*, *IRF8*, *ISG15*, *JAK1*, *NEMO*, *RORC*, *SPPL2A*, *STAT1*, *TBX21*, and *TYK2*) have been reported, defining 32 genetic etiologies due to the allelic heterogeneity at multiple loci (1, 3, 4). The products of these genes are involved in the production of, or response to interferon- $\gamma$  (IFN- $\gamma$ ), which is therefore more a macrophage-activating factor than an anti-viral IFN (5). Most genetic etiologies underlie “isolated MSMD”, with few clinical features other than mycobacterial and related infections. Fewer etiologies underlie “syndromic MSMD”, in which additional pathways other than that governed by IFN- $\gamma$  (e.g. IFN- $\alpha/\beta$ , IL-17A/F) are also disrupted, resulting in one or a few additional clinical phenotypes, infectious or otherwise (e.g. viral or fungal infections) (6-10). Outside the “syndromic MSMD” umbrella, which has somewhat arbitrary boundaries, other inborn errors of immunity (IEI) can underlie mycobacterial disease with a broader range of phenotypes, such as MonoMAC due to inherited GATA2 deficiency, which is invariably associated with monocytopenia and a lack of dendritic cells (DCs) (11-13). The study of MSMD led to the discovery of both the first rare and common monogenic etiologies of TB (14-17). No genetic explanation has yet been found for about half

the cases of MSMD. In this context, we were intrigued by the discovery of two unrelated patients with MSMD or TB displaying intermittent monocytosis.

## Results

### Patients from two unrelated kindreds are homozygous for *ZNFX1* variants

We studied the exomes of two index cases (P1 and P2) — one with MSMD (P1, kindred A, II.2) and the other with severe TB (P2, kindred B, II.1) — and a sibling of P2 (P3, kindred B, II.7), who also displayed the distinctive feature of intermittent monocytosis (P1, P2, and P3), which has never before been reported in any of the patients with known genetic etiologies of MSMD or TB (**Figure 1A, Supplemental Figure 1**). The patients' clinical features are detailed in the **Supplemental data (case reports, Supplemental table 1)**. Two of the patients (P2 and P3) also had unexplained episodes of organomegaly, fever, and thrombocytopenia. However, they were never hospitalized for severe viral disease despite seropositivity for multiple viruses, attesting to previous infections, as detected by phage immunoprecipitation–sequencing (PhIP-Seq) (**Supplemental Figure 2**). P1 is from Iran (kindred A) and is 13 years old, whereas P2 and P3 originate from Morocco and are living in Belgium (kindred B) and are 22 and 11 years old, respectively. The two families were unrelated to each other, but each family was consanguineous. We therefore searched for autosomal recessive (AR) genetic etiologies by testing a hypothesis of genetic homogeneity (i.e. the three patients being homozygous for variants of the same gene), using whole-exome sequencing (WES) data for the three patients. We considered only non-synonymous coding variants that were rare in public databases (minor allele frequency, MAF < 0.01) and absent from our in-house cohort of > 10,000 patients with various infectious disease. This approach identified *ZNFX1* (zinc finger NFX1-type containing 1, NM\_021035.2, GRCh37) as the only candidate gene in the three patients (P1, P2 and P3) (**Figure 1B, Supplemental Figure 3A**). No other genes including known IEI and MSMD/TB

genes (1, 3, 18, 19), presented homozygous rare non-synonymous coding variants (single-nucleotide variant, SNV or copy number variant, CNV) common to the three patients. A brother of P2 and P3 (kindred B, II.6, P4) died at 14 months of age from *Mycobacterium tuberculosis* meningo-encephalitis, suggesting that he shared this recessive phenotype. He was not genotyped because no material was available. The ancestries of these patients were confirmed by principal component analysis (PCA) (**Figure 1C**). Their high homozygosity rates (4.9%, 2.2% and 1.7%), as also shown by WES (20), confirmed parental consanguinity (**Supplemental Figure 3A**). P1 carried a homozygous small deletion of 4 nucleotides (c.4815\_4818del) in *ZNF1*, which was predicted to create a premature stop codon 10 amino acids downstream (p.E1606Rfs\*10) (**Figure 1B**). P2 and P3 carried a homozygous single-nucleotide substitution (c.2876C>G) resulting in a premature stop codon (p.S959\*) (**Figure 1B**).

#### **The two *ZNF1* variants are very rare and predicted to be damaging**

The c.4815\_4818del variant (p.E1606Rfs\*10) is exceedingly rare, has been reported only once before, in the heterozygous state, in South Asia (allele count  $n=1$  in the gnomAD v2.1.1 database; rs775817125; MAF =  $3.98 \times 10^{-6}$ ). The p.S959\* variant is not reported in public databases (gnomAD v2.1.1, BRAVO/TOPmed) or our in-house database consisting of >10,000 exomes, including >1,000 exomes from patients from Northern Africa or the Middle East (**Figure 1D**) (21). Moreover, both variants were predicted to be deleterious, with combined annotation-dependent depletion (CADD) scores of 35 and 40, respectively, well above the corresponding mutation significance cutoff (MSC) for *ZNF1* (99% confidence interval) (22) (**Supplemental Figure 3B**). The p.E1606Rfs\*10 variant is located downstream from the zinc-finger (ZNF) domain, whereas the p.S959\* variant is located within the helicase domain (**Figure 1B**). Finally, Sanger sequencing of *ZNF1* from genomic DNA extracted from whole blood (P1, P2, P3), simian virus 40 (SV40)-immortalized fibroblasts (P1, P2), and Epstein-Barr



virus-immortalized B lymphocytes (EBV-B cells) (P1), confirmed the patients' homozygosity for the corresponding variant (**Figure 1A, Supplemental Figure 3C**). The genotypes of the other individuals are consistent with an AR pattern of inheritance, with incomplete penetrance for MSMD or TB but complete penetrance for monocytosis. Overall, these findings suggest that homozygosity for very rare or private *ZNFX1* variants predicted to be loss-of-function (pLOF) underlies monocytosis and/or mycobacterial diseases in the four patients.

### **The *ZNFX1* gene is under strong negative selection**

*ZNFX1* is a highly conserved helicase protein from the Up-frameshift 1 (UPF1)-like superfamily 2 (SF2) (23). Very little is known about its biological function. It plays a crucial role in RNAi-mediated gene silencing in *Caenorhabditis elegans* (24, 25). In mouse and human cell lines, *ZNFX1* has been reported to act as a cytosolic dsRNA sensor with antiviral activity through interaction with mitochondrial antiviral signaling protein (MAVS) (26). There are no homozygotes for predicted loss-of-function (pLOF) variants in any public database (BRAVO/gnomAD/TOPmed) and there are no other homozygotes for any non-synonymous rare variants of this gene in our in-house database of > 10,000 patients with diverse severe infectious diseases, further suggesting that the variants carried by the patients are disease-causing. The cumulative frequency of heterozygous pLOF variants in public databases is no higher than  $1.70 \times 10^{-4}$  after filtering out variants with low coverage (covered in 50% of individuals) and non-canonical transcripts. There is no major ethnic group in which pLOF variants are less rare. The *ZNFX1* gene has a residual variation intolerance score (RVIS) of -0.96 (placing it in the top 14% of human genes most intolerant to genetic variation), a gene damage index (GDI) of 5.5 (top 29%), and a consensus negative selection (CoNeS) score of -1.31 (top 11%), suggesting that *ZNFX1* is a target of strong negative selection (**Figure 1E-F**) (20, 27, 28). Comparisons with known genes for which variants have been shown to underlie

IEI showed that *ZNFX1* falls at the intersection of the groups of genes underlying AR and autosomal dominant (AD) disorders (20). Overall, these findings suggested that homozygosity for pLOF variants of the negatively selected *ZNFX1* gene would be exceedingly rare in the general population and that the very rare *ZNFX1* pLOF variants observed in these two kindreds would be deleterious, causing monocytosis and/or mycobacterial disease when present in homozygosity, in the patients.

### **Overexpression of the E1606Rfs\*10 and S959\* *ZNFX1* mutants leads to the production of truncated proteins**

The canonical *ZNFX1* mRNA (NM\_021035.2, GRCh37) consists of 14 exons. It encodes a protein of 1,918 amino acids (aa) with a predicted molecular weight (MW) of 220 kDa. We studied the production of the mutant *ZNFX1* proteins by plasmid-mediated overexpression of the corresponding cDNAs in human embryonic kidney (HEK) 293T cells. We generated C-terminal DDK-tagged cDNA constructs for the expression of the two variants, p.E1606Rfs\*10 and p.S959\*. In transient transfection experiments, we evaluated the impact of the two *ZNFX1* variants relative to the wild-type (WT) cDNA. Transfection with p.E1606Rfs\*10 and p.S959\* resulted in the production of abundant *ZNFX1* mRNA, as shown by reverse transcription-quantitative PCR (RT-qPCR) with a probe binding the region spanning the junction between exons 3 and 4 (left) or exons 13 and 14 (right) (**Figure 1G**). SDS-PAGE and western blotting (WB) of cell extracts, followed by immunodetection with a specific monoclonal antibody (mAb) against the N-terminal region of anti-*ZNFX1*, showed that the WT proteins were produced at the expected MW of about 220 kDa. By contrast, overexpression of the p.E1606Rfs\*10 (predicted MW ~179 kDa) and p.S959\* (~106 kDa) alleles resulted in truncated proteins (**Figure 1H**). Using a mAb directed against a C-terminal DDK-tag, we were unable to detect the p.E1606Rfs\*10 and p.S959\* mutant proteins on WB, implying that there

was no re-initiation of translation. Analyses of the nuclear and cytosolic protein fractions showed that the WT protein and mutant proteins lacking one of the three domains (Armadillo [ARM], Helicase, and Zinc-finger [ZNF]) of the ZNFX1 protein were located in the cytoplasm (**Supplemental Figure 3D**). We also tested 25 non-synonymous variants of this gene present in the homozygous state in public databases (gnomAD,  $n=23$  and BRAVO/TOPmed,  $n=2$ ). All were missense and all presented normal protein expression on WB (**Supplemental Figure 3E**). These results suggest that the patients' nonsense and ultra-rare private and frameshift variants encode truncated proteins, whereas all the non-synonymous variants found in the homozygous state in the general population are normally expressed. These findings show that the patients' *ZNFX1* variants strongly alter the nature of the ZNFX1 proteins produced, consisted with the notion that they are deleterious and pathogenic.

### **ZNFX1 colocalizes with cytoplasmic ribonucleoprotein stress granules**

Human *ZNFX1* mRNA is broadly detected in adult tissues, but predominantly in hematopoietic cells (Human Protein Atlas, GTEx, and BioGPS) (29). The pattern of expression of human ZNFX1 protein is not well delineated. Its subcellular distribution is also unclear. *In silico* analyses of its primary structure with various software did not detect known targeting signals for specific subcellular organelles (30). Its helicase and ZNF domains suggest that it is capable of interacting with nucleic acids (26, 31). Human ZNFX1 has been reported to be present at the outer mitochondrial membrane following transient transfection of A549 epithelial cell lines, whereas, in *C. elegans*, worm WT-ZNFX1 was located in germ granules (P-granules) (25, 26). We performed confocal microscopy with a monoclonal antibody (mAb) against ZNFX1 in A549 and HeLa epithelial cells transiently transfected with human WT-*ZNFX1*. We found that ZNFX1 was located within the cytoplasm in HeLa and A549 cells, with two different non-exclusive fluorescence patterns, a diffuse and a punctuated distribution (**Figure 2A and**

**Supplemental Figure 4).** ZNFX1 did not colocalize with the endoplasmic reticulum, peroxisomes, endosomes, lysosomes, membrane-associated Golgi apparatus, or mitochondria (**Supplemental Figure 4A**). A similar localization was confirmed in SV40 fibroblasts stimulated with poly(I:C) from a healthy control, whereas no ZNFX1 protein was detected in SV40 fibroblasts of P2 using a mAb recognizing the N-terminal part of ZNFX1, from which the recognized epitope is upstream the mutation site (**Supplemental Figure 4B**). We then tested the colocalization of WT-ZNFX1 with membrane-less ribonucleoprotein (RNP) granules in transiently transfected A549 and HeLa cells. We found that ZNFX1 localized to stress granules formed upon transfection, which is typical of RNA-binding proteins, as shown using antibodies against two stress granule markers, G3BP1 and TIA1 (**Figure 2A and Supplemental Figure 4C**) (32-35). Moreover, transient transfection of WT-ZNFX1 into A549 and HeLa cells induced stress granule formation in about half of the transfected cells. By comparison, stress granules were observed in less than 1% of the cells transfected with an empty vector (EV) (**Figure 2A and Supplemental Figure 4C-D**). Similarly, endogenous ZNFX1 localized in arsenite-induced stress granules in SV40 fibroblasts from healthy control and activated THP1 cells (**Figure 2B-C**). However, human ZNFX1 did not localize in P-bodies, as shown using antibodies against DCP1a. The striking juxtaposition of DCP1a-containing P-bodies and ZNFX1-containing stress granules has been observed in many studies (**Supplemental Figure 4E**) ([doi: 10.1242/jcs.01692](https://doi.org/10.1242/jcs.01692)) (37). These findings suggest that ZNFX1 is an RNA-binding protein that localizes to stress granules.

### ***ZNFX1* expression in the patients' cell lines**

We assessed the impact of the homozygous *ZNFX1* mutations on both mRNA and protein levels in the patients' cells, using both immortalized non-hematopoietic (SV40 fibroblasts, P1 and P2) and hematopoietic (EBV-B cells, P1, not available for P2) cell lines. No

cell line was available for P3 and P4. We first amplified the WT and mutant full-length cDNAs. We performed RT-quantitative PCR (RT-qPCR) with two sets of probes for the *ZNFX1* mRNA. Comparison with cells from healthy controls showed that SV40 fibroblasts and EBV-B cells from P1 displayed normal levels of *ZNFX1* mRNA production (**Figure 2A-B**). By contrast, the SV40 fibroblasts of P2 contained about 5% the level of *ZNFX1* mRNA found in the wild type (**Figure 2C**), suggesting that nonsense-mediated mRNA decay was occurring. We then used SDS-PAGE, followed by western blotting with a mAb against the N-terminus of ZNFX1, to assess the levels of endogenous ZNFX1. The WT protein was produced at the expected MW. By contrast, SV40 fibroblasts and EBV-B cells from P1 produced a mutant protein with a MW lower than that of the WT protein, consistent with truncation. Moreover, SV40 fibroblasts from P2 contained no detectable ZNFX1 protein (**Figure 2C-D**). However, protein production was rescued by introducing the WT *ZNFX1* cDNA by lentiviral transduction, confirming that the p.S959\* variant leads to a loss of expression (**Supplemental Figure 3F**). Overall, these results show that homozygosity for the p.E1606Rfs\*10 and p.S959\* *ZNFX1* variants results in the production of truncated proteins in SV40 fibroblasts and EBV-B cells from P1 and a lack of detectable protein in SV40 fibroblasts from P2, respectively. Together with our previous findings, these data suggest that at least three of these patients, and possibly all four, have AR complete ZNFX1 deficiency.

### **Frequency of lymphoid and myeloid cells among the cells of ZNFX1-deficient patients**

We analyzed the impact of ZNFX1 deficiency on leukocyte development. Complete blood counts on fresh samples from the three patients tested (P1, P2, P3) revealed peripheral leukocytosis with intermittent monocytosis and variable neutrophilia and lymphocytosis, even in the absence of clinical infection (**Figure 3A**). No leukocyte counts were available for P4

(already deceased). Bone marrow aspiration in P2 at the age of 12 years showed that all hematopoietic lineages were present, with multiple cells of the monocyte lineage (42%) bearing lobular nuclei without chromosomal abnormalities (**Supplemental Figure 1**). Abundant monocytes were detected on concomitant blood smears (**Supplemental Figure 1**). We then studied cryopreserved peripheral blood mononuclear cells (PBMCs) from P1, P2, and P3 by conventional flow cytometry and mass cytometry (cytometry by time-of-flight, CyTOF) (**Figure 3B**). At the time of sampling, P1 and P2 (aged 12 and 15 years, respectively) had high relative and absolute numbers of monocytes in complete blood counts (**Figure 3A**). Flow cytometry and CyTOF showed that the proportions of CD4<sup>+</sup> and CD8<sup>+</sup> T cells and B cells among PBMCs were normal, relative to age-matched controls (**Figure 3 B-E**). The proportions of naive CD4<sup>+</sup> T cells and memory CD4<sup>+</sup> and CD8<sup>+</sup> subsets, regulatory T cells (Tregs), and  $\gamma\delta$  T cells were also normal (**Figure 3C-D-F**). The proportion of NK cells was low among the PBMCs of the three patients tested, with a low frequency of CD56<sup>dim</sup> NK cells and a normal frequency of CD56<sup>bright</sup> NK cells (**Figure 3G**). The proportions of CD4<sup>+</sup> and CD8<sup>+</sup> mucosal associated invariant T (MAIT) cells were conserved in the three patients (**Figure 3H**). At the time of sampling, the proportion of total monocytes had not increased in any of the patients tested, as detected by CyTOF. Two of the three monocyte subpopulations, classical (CD14<sup>+</sup>CD16<sup>-</sup>) and intermediate (CD14<sup>+</sup>CD16<sup>+</sup>) monocytes, were in the range of healthy controls, whereas the proportion of non-classical (CD14<sup>dim</sup>CD16<sup>+</sup>) monocytes was low (**Figure 3I**). The frequency of basophils and eosinophils was normal (**Figure 3J-K**). The proportions of total dendritic cells (DCs) and of conventional (cDC1 and cDC2) and plasmacytoid (pDC) DCs were normal on CyTOF, in all three patients tested, and on flow cytometry for fresh PBMCs from P1 (**Figure 3L** and data not shown). Overall, the development of other myeloid and lymphoid subsets was largely normal at the time of sampling among the patients with inherited ZNF1 deficiency tested.

### **Normal production of IFN- $\gamma$ by ZNFX1-deficient lymphocytes**

IFN- $\gamma$  is essential for protective immunity to mycobacteria in humans (4, 38, 39). The related IL-12 and IL-23 cytokines, and secreted ISG15, are required for human antimycobacterial immunity and are induced by IFN- $\gamma$  (6, 15, 40). An impaired production of, or response to IFN- $\gamma$  is characteristic of MSMD patients (1, 3). Among leukocyte subsets, human ZNFX1 is most abundantly expressed in neutrophils, monocytes, and macrophages (ProteinAtlas and BioGPS databases). Mouse ZNFX1 is also more abundant in macrophages, but the antimycobacterial immunity of ZNFX1-deficient mice has not been evaluated (26). We found that *ZNFX1* transcription was induced after BCG infection, more so than after stimulation with phorbol 12-myristate 13-acetate (PMA) in the THP1 monocyte cell line (**Supplemental Figure 5A**). We also assessed the impact of ZNFX1 deficiency on IFN- $\gamma$  production by fresh lymphocytes. Whole-blood IFN- $\gamma$  production after stimulation with BCG alone or BCG plus IL-12 was normal in P1 (data not available for the other patients) (**Supplemental Figure 5B**). The production of IFN- $\gamma$  and TNF- $\alpha$  after stimulation with BCG alone, BCG plus IL-12, BCG plus IL-23, or PMA-ionomycin was also normal for cryopreserved PBMCs (**Figure 4A, Supplemental Figure 5C**). In addition, the proportion of innate (NK cells), “innate-like” (iNKT, MAIT, and  $\gamma\delta$  T cells), and adaptive (CD4<sup>+</sup> and CD8<sup>+</sup> T cells) lymphocytes producing IFN- $\gamma$  was normal following stimulation with BCG alone, BCG plus IL-12, or BCG plus IL-23, as measured by flow cytometry (**Figure 4B-F**). Overall, these findings indicate that the development of the major lymphocyte subsets and their IFN- $\gamma$  production were normal in ZNFX1-deficient patients.

### **Normal response to IFN- $\gamma$ in the cells of ZNFX1-deficient patients**

We then tested cellular responses to IFN- $\gamma$ . *ZNFX1* transcription is increased by IFN- $\gamma$  in human monocyte-derived macrophages (MDMs) (41). We investigated whether *ZNFX1* deficiency led to an impaired IFN- $\gamma$  response in primary cells and cell lines from the patients. IL-12p40 secretion by whole blood following IFN- $\gamma$  stimulation was normal in P1, although its induction by BCG or BCG+IFN- $\gamma$  was in the lower range of controls (**Figure 4G**). Moreover, the production of IL-12p40 and IL-12p70, and of TNF- $\alpha$  was normal after stimulation with phorbol 12, 13-dibutyrate (PDBu) in EBV-B cells from P1 (**Figure 4H** and **Supplemental Figure 5E-F**). Early responses to IFN- $\gamma$ , as evaluated by STAT1 phosphorylation in EBV-B cells (P1), and late responses to IFN- $\gamma$ , as evaluated by HLA-DR induction in SV40 fibroblasts from P1 and P2, were normal (**Figure 4I-J**). The production of reactive oxygen species (ROS) by neutrophils from P1 and P2 in response to PMA was normal, as was the production of NADPH oxidase complex subunits and cytochrome *b* by EBV-B cells (data not shown). Overall, leukocytes from *ZNFX1*-deficient patients responded normally to IFN- $\gamma$ , and immortalized hematopoietic and non-hematopoietic cell lines from patients displayed apparently normal responses to IFN- $\gamma$ .



## Discussion

We report here four patients from two unrelated kindreds, originating from Iran and Morocco, with a novel form of ‘syndromic’ MSMD or TB, associated with intermittent but marked monocytosis. The patients have AR ZNFX1 deficiency. Two of these patients also had recurrent and unexplained episodes of fever, thrombocytopenia, and organomegaly. ZNFX1 is ubiquitously expressed, but its function remains elusive. It would not, therefore, be surprising for these and, perhaps, other manifestations to be documented as clinical phenotypes when more ZNFX1-deficient patients are characterized. Penetrance for MSMD or TB is difficult to calculate. Only one of the four patients was vaccinated with BCG and he had clinical disease. It is unknown whether the patients are prone to clinical disease caused by environmental mycobacteria, another defining feature of MSMD (1, 2, 42). Two patients had severe TB and the fourth did not suffer from any mycobacterial disease. Severe mycobacterial disease occurred at the ages of three months (P1, BCG-osis), 11 years (P2, TB), and 14 months (P4, TB). The three surviving patients are now 13 years (P1), 22 years (P2), and 11 years (P3) old. P3 had not developed mycobacterial disease by the age of 11 years and had not received the BCG vaccine. His exposure to *M. tuberculosis* is unknown. The penetrance of ZNFX1 deficiency for TB is probably greater than that for MSMD, if only because *M. tuberculosis* is about 1,000 times more virulent than BCG (15-17).

The vast majority of MSMD patients have normal counts of myeloid cells, except patients with AD partial IRF8 and AR complete SPPL2a deficiencies, which present defects of both cDC1s and cDC2s and of cDC2s alone, respectively (43, 44). In addition to MSMD, patients with AR complete IRF8 deficiency have monocytopenia associated with a complete loss of DCs (43). Monocytopenia is also seen in MonoMAC caused by germline heterozygous *GATA2* mutations, which is characterized by a wide range of clinical manifestations, including mycobacterial disease (13, 45, 46). Monocytosis can be found during mycobacterial disease, in

the course of autoimmune conditions, such as Ras-associated autoimmune leukoproliferative disorder (RALD), or associated with various myeloid neoplasms (47-49). The monocytosis of the ZNFX1-deficient patients is unlikely to be due to their mycobacterial disease, because their monocyte counts remained high up to five years after the clinical remission of mycobacterial disease. In P1, blood monocytosis was associated with bone marrow monocytosis, as reported twice in studies performed during acute episodes of fever, that of which resolved. By contrast to clonal disorders, such as juvenile myelomonocytic leukemia (JMML, which frequently present with monocytosis, cytopenia, and organomegaly), the bone marrow of P2 presented no cellular dysplastic features or chromosomal abnormalities (50, 51). Furthermore, mycobacterial infection is uncommon in patients with JMML (52). AR ZNFX1 deficiency is, therefore, a genetic etiology of MSMD or TB associated with intermittent monocytosis. The mechanisms underlying monocytopoiesis in these patients remain to be studied.

Given that impaired production of, or response to IFN- $\gamma$  is the defining characteristic of the known genetic etiologies of MSMD, we checked for these cellular phenotypes in primary cells and cell lines from the patients. We found no evidence of any major defect of IFN- $\gamma$  production by the various subsets of lymphoid cells. We also found no evidence of any major disruption of the IFN- $\gamma$  response pathway in whole blood and cell lines. However, ZNFX1 is expressed predominantly in myeloid cells, particularly in neutrophils and monocytes, and its transcription is induced following the infection of THP1 cells with BCG. Both the mycobacterium- and IFN- $\gamma$ -responsive pathways should be studied in the various subsets of myeloid cells *ex vivo* or with iPSC-derived myeloid cells *in vitro* (53). All the genes involved in MSMD affect the response and/or production of IFN- $\gamma$ . It is tempting to speculate that ZNFX1 may affect the production of IFN- $\gamma$ -inducing cytokines, such IL-12p70, IL-23, and ISG15, by certain subsets of myeloid cells. It would also be of interest to test ZNFX1-deficient mice for antimycobacterial immunity. ZNFX1 is the first product of an MSMD gene shown to

have RNA-binding activity. If an IFN- $\gamma$ -related cellular phenotype were identified, it would be essential to try to understand the causality of ZNFX1 defects. This will involve deciphering the mechanism by which a protein bound to RNAs can disrupt IFN- $\gamma$ -related immunity, or other mechanisms of anti-mycobacterial immunity (54, 55).

Our findings suggest that ZNFX1 is recruited in stress granules, at least in A549, HeLa, THP1 cells and SV40 fibroblasts. Stress granules can associate with P-bodies, but the components, structures and functions of stress granules and P-bodies are different (56, 57). Interestingly, T. Ishidate and coworkers previously reported the localization of ZNFX1 in germline-specific membrane-less RNP organelles called P-granules in *C. elegans* (24). While this protein was not detected in P-bodies, we found that ZNFX1 induced stress granules formation, which is typical of RNA-binding proteins (32-35). Some cellular environment conditions, such as oxidative stress, heat shock, hyperosmolarity, viral infection and UV irradiation, can trigger the assembly of stress granule components (57-59). Further studies will be required to determine whether the localization of ZNFX1 in stress granules is involved in protective immunity to mycobacteria. Finally, it is intriguing that our patients did not suffer from severe viral illnesses, whereas mouse ZNFX1 has been reported to be important for antiviral immunity via the sensing of dsRNA (26). More patients should be identified, their clinical histories analyzed and their cells tested, before any firm conclusions are drawn. Overall, our study indicates that human ZNFX1 is a protein recruited in stress granules. Human ZNFX1 is essential for monocyte homeostasis and protective immunity to mycobacteria, via mechanisms potentially involving myeloid cells, as the patients described here displayed monocytosis and ZNFX1 levels are highest in monocytes. Further studies are required to delineate more clearly the essential and redundant functions of human ZNFX1 at the cellular, immunological, and clinical levels.



## **Materials and methods**

### **Patient recruitment and ethnics**

Clinical history and biological specimens were obtained from the referring clinicians, with the signed consent of the patients, parents and siblings participating in the study. All the experiments involving human subjects conducted in this study were performed in accordance with institutional, local and national ethical guidelines. Approval was obtained from the French Ethics Committee “Comité de Protection des Personnes”, the French National Agency for Medicine and Health Product Safety (ANSM), the “Institut National de la Santé et de la Recherche Médicale” (INSERM) in France and the Rockefeller University Institutional Review Board (IRB), New York, USA.

### **Genomic DNA, WES and Sanger sequencing**

Genomic DNA (gDNA) was extracted from peripheral blood mononuclear cells (PMBC) after Ficoll-Paque Plus gradient purification, or from whole blood with the iPrep PureLink gDNA Blood kit and iPrep Instruments (Life Technologies, Thermo Fisher Scientific). WES was performed on gDNA from patients (P1-P3), as previously described (4). Briefly, an adapter-ligated library was prepared with the TruSeq DNA Sample Prep Kit (Illumina). Exome capture was performed with the SureSelect Human All Exon 50 Mb kit (Agilent Technologies). Paired-end sequencing was performed on an Illumina HiSeq 2000 (Illumina), generating 100-base reads. The sequences were aligned with the human genome reference sequence (hg19 build), with the Burrows-Wheeler Aligner (60). Downstream processing was performed with the Genome Analysis Toolkit (GATK), SAMtools (62), and Picard Tools (<http://picard.sourceforge.net>). Substitution and indel calls were made with GATK Unified Genotyper and GATK IndelGenotyperV2, respectively. All calls with a Phred-scaled single-nucleotide polymorphism quality  $\leq 20$  and a read coverage  $\leq 2$  were filtered out. All

mutations found in *ZNF1* were confirmed by Sanger sequencing on genomic DNA. Familial segregation was analyzed if DNA samples from relatives were available. Sanger sequencing was performed on amplified PCR products purified by ultracentrifugation through Sephadex G-50 Superfine resin (Amersham-Pharmacia-Biotech) and sequenced with the Big Dye Terminator 3.1 Cycle Sequencing Kit on an ABI Prism 3700 apparatus (Applied Biosystems). Sequence files and chromatograms were analyzed with Genalys 2.8 software (CNG, France; <http://software.cng.fr>).

### **Cell culture, stimulation and flow cytometry**

EBV-B cells were cultured in RPMI 1640 medium (GIBCO BRL) supplemented with 10% heat-inactivated pooled fetal bovine serum (FBS) (GIBCO BRL), referred to as complete RPMI 1640. HEK293T cells and SV40 fibroblasts were cultured in DMEM (GIBCO BRL) supplemented with 10% FBS. Cells were grown at 37°C, under an atmosphere containing 5% CO<sub>2</sub>. For the study of IL-12p40/IL-12p70/TNF- $\alpha$  production by EBV-B cells, 2 x 10<sup>6</sup> cells in 1 mL RPMI-2% FCS were stimulated by incubation for 24 h with 10<sup>-7</sup>M PDBu (Sigma-Aldrich) (63). EBV-B cells or SV40 fibroblasts were washed in phosphate-buffered saline (PBS) and dispensed into a 24-well plate for labeling. Aqua (Live/Dead Fixable Dead Cell Stain kit from Invitrogen) staining was performed to exclude dead cells. The cells were then left unstimulated, or were stimulated by incubation with IFN- $\gamma$  (10<sup>5</sup> IU/mL, Imukin), or IFN- $\alpha$ 2b (10<sup>5</sup> IU/mL, IntronA) for 20 min. The reaction was then stopped by adding cold PBS, and the cells were harvested with trypsin and stained directly. Intracellular staining was performed with the Cytotfix/Cytoperm Plus Fixation/Permeabilization kit (BD) with anti-STAT1-PE (BD), or anti-Y701-pSTAT1-Alexa468 (BD) antibodies or an equivalent concentration of isotype-matched control mAb (Becton Dickinson) in 2% FBS in PBS, for 1 h at 4°C. Compensation was

performed on single-stained non-stimulated samples. Staining was assessed on a Gallios Flow cytometer (Beckman Coulter), and the results were analyzed with FlowJo v10 (Tree Star).

SV40 fibroblasts were plated at a density of  $10^5$  cells in 1 mL DMEM-10% FBS in 12-well plates. The following day, they were left unstimulated or were stimulated with recombinant IFN- $\alpha$ 2b (Introna, MSD) or recombinant IFN- $\gamma$  (Imukin). Forty-eight hours later after stimulation, cells were harvested with trypsin, and stained with FITC-HLA-DR antibody (clone L243, #307604, Biolegend). Cells were also stained with the Aqua Dead Cell Stain kit (#L34957 Thermo Fisher Scientific). Cells were acquired on a Beckman Coulter Gallios flow cytometer and analyzed with FlowJo Software.

#### **Site-directed mutagenesis, transient and stable transfection**

A DDK-tagged *ZNFX1* cDNA plasmid was obtained from Origene (#RC214589, Origene). Constructs carrying single-nucleotide mutant alleles were generated from this plasmid by mutagenesis with appropriate primers, with the Pfu Ultra II Fusion HS DNA (#600674, Agilent) polymerase. They were then digested with *DpnI* (#R0176L, New England Biolab). Site-directed deletions were created with CloneAmp HiFi (Takara, #639298), and the blunt ends were 5'-phosphorylated with the T4 DNA polymerase (#E1201S, New England Biolab), and ligated with the Quick ligation kit (#M2200S, New England Biolabs). Plasmids were amplified in competent cells of *E. coli* (#C3019H, New England Biolab) and purified with the Maxiprep kit (#12162, Qiagen). HEK293T cells were transiently transfected with the various constructs, with X-tremeGENE9 (#XTG9-RO, Roche), used in accordance with the manufacturer's instructions.

The WT coding sequence of *ZNFX1* was inserted into pTRIP-SSFV-deltaNGFR-2A. For lentivirus production, HEK293T cells were transfected with 1.6  $\mu$ g pTRIP-SSFV-DNGFR-2A-ZNFX1-WT, 0.2  $\mu$ g pCMV-VSV-G (Addgene #8454), 0.2  $\mu$ g pHXB2 (NIH-AIDS Reagent

Program #1069) and 1  $\mu\text{g}$  psPAX2 (Addgene #12260), with X-treme gene 9 (Roche), according to the manufacturer's instructions. Supernatants were harvested after 24 h and 8  $\mu\text{g}/\text{mL}$  protamine sulfate was added. The lentiviral suspension obtained was used to transduce  $2 \times 10^5$  SV40 fibroblasts by spinoculation at  $1,200 \times g$  for 2 h. The transduced cells were subjected to MACS purification with anti-CD271 microbeads (Miltenyi Biotec), and the purified cells were used for further experiments. Transduction was confirmed by flow cytometry with an anti-CD271-PE antibody (BD Bioscience).

### **Western blot**

Total protein extracts were prepared by mixing cells with lysis buffer (50 mM Tris-HCl pH 7.4, 150 mM NaCl, 0.5% Triton X-100, and 2 mM EDTA) supplemented with protease inhibitors (Complete, Roche), phosphatase inhibitor cocktail (PhosphoStop, Roche), 0.1 mM dithiothreitol (DTT, Life Technologies), phenylmethylsulfonyl fluoride (PMSF) and incubating for 30 min on ice. The cytoplasmic and nuclear fractions of the cells were separated with NE-PER nuclear and cytoplasmic extraction reagents (Thermo Fisher Scientific, #78835). Protein fractions were separated by SDS-PAGE and the resulting bands were electrotransferred onto PVDF membranes. The membrane was blocked by incubation in TBS supplemented with 0.1% Tween 20 and 5% skimmed milk powder for 60 min at room temperature and incubated with antibodies against ZNFX1 (Abcam, ab179452), HRP-DDK (Sigma-Aldrich, #A8592), tubulin (Cell Signaling, sc-239448), and HRP-lamin A/C (Santa Cruz, sc-376248). Membranes were washed several times in 0.05% Tween-20 in PBS, and antibody binding was detected by incubation with horseradish peroxidase-conjugated anti-rabbit or anti-mouse secondary antibodies (GE Healthcare), by enhanced chemiluminescence (GE Healthcare).



### **RNA extraction, RT-qPCR and cDNA**

Total RNA was extracted with the RNeasy Mini Kit (#74104, Qiagen), according to the manufacturer's instructions. Reverse transcription was performed on 1 µg of RNA with random primers and the High-Capacity RNA-to-cDNA Kit (Applied Biosystems), according to the manufacturer's protocol. Quantitative PCR was then performed with the TaqMan™ Fast Universal PCR Master Mix (2X), No AmpErase™ UNG (Thermo Fisher Scientific, #4352042) and the following probes, all from Thermo Fisher Scientific: *ZNFX1* exons 13-14 (Hs01105231\_m1), *ZNFX1* exons 3-4 (Hs01105222\_m1), *GUSB* (#1702016), in an ABI PRISM® 7700 Sequence Detection System. The relative expression levels of the genes were calculated with the formula  $2^{-\Delta C_t}$ , and the results were normalized against the levels of mRNA for the housekeeping gene encoding β-glucuronidase (*GUS*).

### **Whole-blood activation ELISA for cytokines**

Whole-blood samples were collected from healthy controls (fresh blood and travel blood) and patients, in heparin-containing collection tubes (63, 64). These samples were diluted 1:2 in RPMI 1640 (GibcoBRL). Diluted blood samples were then dispensed into five wells (1 mL/well) of a 48-well plate (Nunc). The samples were incubated for 48 h at 37°C, under an atmosphere containing 5% CO<sub>2</sub>, and under three different sets of activation conditions: with medium alone, with live BCG (*M. bovis*-BCG, Pasteur substrain), or with BCG plus recombinant (rh) IL-12 (20 ng/mL; R&D Systems), or BCG plus IFN-γ (Imukin). The cell culture supernatant or whole blood was collected for determinations of IL-12p40 (#DP400, R&D Systems) or IFN-γ (Sanquin) by ELISA, according to the kit manufacturer's protocol.

### **Confocal microscopy**

HeLa or A549 cells were plated on chambered coverslips (#80826, iBidi) and were left untransfected or were transiently transfected with the *ZNFXI* cDNA plasmid or an empty pCMV6 vector for 24 hours. SV40 fibroblasts or THP1 cells were plated on chamber coverslips and left stimulated or not with BCG or poly(I:C), respectively, for 24 hours. The cells were fixed in 4% formaldehyde in phosphate-buffered saline (PBS), pH 7.4. Cells were incubated overnight at 4°C with primary antibody: mouse anti-G3BP (Abcam #ab56574), anti-DCP1A (Abnova #H00055802-M06), anti-RAB7 (Abcam #ab50533), anti-PMP70 (Sigma #SAB4200181), anti-LAMP-2 (Santa Cruz # sc-18822), anti-EEA1 (BD # 610457), anti-TIA1 (Santa Cruz #sc-166247) and rabbit anti-ZNFXI (Abcam, ab179452) antibodies. The cells were washed three times with PBS 1X and stained by incubation with secondary antibodies for 1 h at room temperature (goat anti-rabbit IgG Alexa Fluor 488 (#A-11034); goat anti-mouse IgG Alexa Fluor 633 (#A-21052)) and before mounting in Prolong-gold and visualization by confocal microscopy (×63 oil immersion lens).

### **Immunophenotyping of leukocytes by mass cytometry**

We performed mass cytometry (cytometry by time-of-flight, CyTOF) with two different antibody panels (termed as regular surface and myeloid panels hereafter) (3, 65). For the regular surface panel, we analyzed PBMCs from 37 healthy adult controls and nine healthy age-matched controls (aged from one to 17 years) from diverse ethnic backgrounds, and three patients (P1, P2 and P3) with homozygous *ZNFXI* mutations in seven batches of experiments performed on different dates. For the myeloid panel, we analyzed PBMCs from 19 healthy adult controls, six healthy age-matched controls (aged from one to 17 years) from diverse ethnic backgrounds, P1, P2, and P3 in five batches of experiments performed on different dates. In particular, the three *ZNFXI*-deficient patients were studied with eight and three healthy adult

controls in a single batch of regular surface and myeloid panel experiments, respectively. Freshly thawed PBMCs ( $1.0 - 1.5 \times 10^6$  cells per panel) were incubated with Fc block and stained with a panel of metal-conjugated antibodies obtained from Fluidigm or through customized conjugation. The regular surface panel consisted of the following antibodies: anti-CD45-89Y, anti-CD57-113In, anti-CD11c-115In, anti-CD33-141Pr, anti-CD19-142Nd, anti-CD45RA-143Nd, anti-CD141-144Nd, anti-CD4-145Nd, anti-CD8-146Nd, anti-CD20-147Sm, anti-CD16-148Nd, anti-CD127-149Sm, anti-CD1c-150Nd, anti-CD123-151Eu, anti-CD66b-152Sm, anti-PD-1-153Eu, anti-CD86-154Sm, anti-CD27-155Gd, anti-CCR5-156Gd, anti-CD117-158Gd, anti-CD24-159Tb, anti-CD14-160Gd, anti-CD56-161Dy, anti- $\gamma\delta$ TCR-162Dy, anti-CRTH2-163Dy, anti-CLEC12A-164Dy, anti-CCR6-165Ho, anti-CD25-166Er, anti-CCR7-167Er, anti-CD3-168Er, anti-CX3CR1-169Tm, anti-CD38-170Er, anti-CD161-171Yb, anti-CD209-172Yb, anti-CXCR3-173Yb, anti-HLA-DR-174Yb, anti-CCR4-176Yb, and anti-CD11b-209Bi antibodies. The myeloid panel consisted of the following antibodies: anti-CD45-89Y, anti-HLA-ABC-113In, anti-CD11c-115In, anti-CD33-141Pr, anti-CD19-142Nd, anti-CD45RA-143Nd, anti-CD141-144Nd, anti-CD4-145Nd, anti-CD8-146Nd, anti-CLEC9A-147Sm, anti-CD16-148Nd, anti-Fc $\epsilon$ RI $\alpha$ -149Sm, anti-CD1c-150Nd, anti-CD123-151Eu, anti-CD66b-152Sm, anti-CD83-153Eu, anti-CD86-154Sm, anti-CD27-155Gd, anti-PD-L1-156Gd, anti-CD163-158Gd, anti-CD103-159Tb, anti-CD14-160Gd, anti-CD56-161Dy, anti-CD64-162Dy, anti-CD40-164Dy, anti-CD169-166Er, anti-CD117-167Er, anti-CD3-168Er, anti-CX3CR1-169Tm, anti-CD38-170Er, anti-CD207-171Yb, anti-CD206-172Yb, anti-HLA-DR-174Yb, anti-Axl-175Lu, anti-CD209-176Yb, and anti-CD11b-209Bi antibodies. The stained cells were washed, fixed and permeabilized with barcode permeabilization buffer (Fluidigm), and barcoded with Fluidigm's Cell-ID 20-Plex Pd Barcoding Kit. Samples were then washed and pooled into a single tube. Dead cells and doublets were excluded by staining the cells with a rhodium-based dead cell exclusion intercalator (Rh103) before fixation and cationic iridium

nucleic acid intercalators (Ir191 and Ir193) after fixation. After surface staining, the samples were fixed and stored until acquisition on a Helios mass cytometer (Fluidigm).

We investigated the immunophenotype of the ZNFX1-deficient patients, by combining data from seven batches of experiments. We manually inspected the data from each batch separately, and computationally compared immunophenotypes across batches in an objective and unbiased manner, with iMUBAC (65). Briefly, this method is a combination of high-dimensional batch correction, unsupervised clustering, and batch-specific cell-type classification through machine learning. Data from each of the samples were first preprocessed for the automatic exclusion of dead cells and doublets. Cells from healthy controls (but not the ZNFX1-deficient patients) were then used for high-dimensional batch correction with *Harmony* (66). Data were down-sampled to 200,000 cells per batch before batch correction. Unsupervised clustering was then performed on the batch-corrected marker expression values, with the *FlowSOM* and *ConsensusClusterPlus* packages in *Bioconductor* (67, 68). Sixty clusters were retained after metaclustering. A batch-specific cell-type classifier was trained on the uncorrected expression values and cell-type annotations. We randomly sampled a maximum of 100 cells per cluster to improve computation efficiency and to alleviate class imbalance issues, as some of the cell types are much rarer than others. An extremely randomized tree algorithm was employed, with *mtry* and *numRandomCuts* hyperparameters tuned for each batch (69). Classifiers were trained through five rounds of 10-fold cross-validation with internal upsampling. Internal accuracy during cross-validation systematically exceeded ~90%. The trained classifier was then applied to all cells, including the patients' cells, for probabilistic cell type determination. Finally, each cluster was inspected manually, identified, and merged on the basis of marker expression patterns, if necessary, to “translate” the assigned clusters into cell types. For visualization purposes, cells from one healthy adult control and three ZNFX1-deficient patients were used to generate Uniform Manifold Approximation and Projection

(UMAP) plots. Data were down-sampled to 100,000 cells per individual. All available markers were used for dimension reduction. Figures are color-coded according to the cell types identified through the unsupervised clustering approach described above. All analyses were performed with R v.4.0.

### **Stimulation of PBMCs with live BCG infection for cytokine production**

This experiment was performed in four batches, on four dates. The data from the four batches were compiled for the final analysis. PBMCs from adult healthy donors, age-matched healthy donors (1 – 17 yo) and P1 – P3 were thawed, resuspended in RPMI 10% FBS and counted. Cells (300,000 per well in 96-well U-bottomed plates) were plated at a density of  $1.5 \times 10^6$  cells/ml. PBMCs from P1 and P2 were plated in duplicated wells for all conditions but BCG+IL-12 and BCG+IL-23 conditions were PBMCs from P1 and PBMCs from P3 were plated in triplicate. Cells were stimulated in the presence and absence of live *M. bovis*-BCG at a MOI=1, and in the presence and absence of recombinant IL-12 (5 ng/mL, R&D) or recombinant IL-23 (10 ng/mL, R&D). Golgiplug (BD Biosciences) was added to each well after 40 h of stimulation. Eight hours later, supernatants were harvested for cytokine determinations in a 13-plex Legendplex assay (BioLegend), and cells were collected by centrifugation for FACS staining. In brief, cells were first stained with the Zombie NIR Viability kit (BioLegend) for 15 min. They were then stained with FcBlock (Miltenyi Biotec), anti- $\gamma\delta$ TCR-alexa 647 (BioLegend), anti-CD3-V450 (BD Biosciences), anti-CD56-BV605 (BioLegend), anti-CD4-BUV563 (BD Biosciences), anti-V $\delta$ 1TCR-FITC (Miltenyi Biotec), anti-CD8-BUV737 (BD Biosciences), anti-V $\delta$ 2TCR-APC/Fire750 (BioLegend), anti-CD20-BV785 (BioLegend), anti-V $\alpha$ 7.2-Alexa 700 (BioLegend), MR1-5-OP-RU-tetramer (NIH tetramer core facility), anti-V $\beta$ 11-APC (Miltenyi Biotec), and anti-iNKT-BV480 (BD Biosciences) antibodies for 30 minutes. The stained cells were fixed with the

FOXP3/Transcription Factor Buffer set (Thermo Fisher Scientific) and intracellularly stained with anti-IFN- $\gamma$ -BV711 (BioLegend) and anti-TNF- $\alpha$ -BV510 (BioLegend) antibodies in Perm/Wash buffer. Cells were acquired on a CyTek Aurora spectral flow cytometer and the data were analyzed with Cytobank.

### **Phage immunoprecipitation-sequencing (PhIP-Seq)**

For antibody profiling by PhIP-Seq, plasma samples were obtained from two patients (P1, P2). For comparison, and as additional controls, we also tested 10% liquid IVIg from pooled human plasma (Privigen® CSL Behring AG) and human IgG-depleted serum (Supplier No HPLASERGF5ML, Molecular Innovations, Inc.). The total IgG levels in the plasma samples were determined with a Human IgG total ELISA Ready-SET-Go kit (Thermo Fisher Scientific). Diluted plasma samples containing approximately 4  $\mu$ g of total IgG were incubated at 4°C overnight with  $2 \times 10^{10}$  plaque-forming units (PFUs) of a modified version of the original PhIP-Seq phage library. This modified T7 phage library was used to display a total of 115,753 peptides, each 56 amino acids (aa) long, including the same viral peptides as the original PhIP-Seq phage library and additional peptides derived from the protein sequences of various microbial B-cell antigens and allergens made available by the IEDB ([www.iedb.org](http://www.iedb.org)). Subsequent steps were performed as previously described (4).

### **Statistical methods**

Statistical analysis was performed with GraphPad Prism, version 7.02 (GraphPad Software). A *p* value of less than 0.05 was considered statistically significant.

### **Web resources**

CADD, <https://cadd.gs.washington.edu/>

gnomAD Browser, <https://gnomad.broadinstitute.org/>

### **Acknowledgments and funding sources**

We would like to thank to Jie Chen and David Langlais for helpful discussions, and Yelena Nemirovskaya, Christine Rivalain, Dominick Papandrea and Lazaro Lorenzo for administrative support. We also thank Stephen Elledge (Brigham and Women's Hospital, Harvard University Medical School) for kindly providing the VirScan phage library used in this study. This research was supported in part by a grant from the National Institute of Allergy and Infectious Diseases (grant number R37AI095983), the National Center for Research Resources and the National Center for Advancing Sciences of the National Institutes of Health (grant number UL1TR001866), the Yale Center for Mendelian Genomics funded by the National Human Genome Research Institute(UM1HG006504), the GSP Coordinating Center (U24HG008956), and the High Performance Computing Center (S10OD018521), The Rockefeller University, the St. Giles Foundation, Institut National de la Santé et de la Recherche Médicale (INSERM), University of Paris, Sidra Medicine (SDR400048), the Integrative Biology of Emerging Infectious Diseases Laboratory of Excellence (ANR-10-LABX-62-IBEID), the French Foundation for Medical Research (FRM) (EQU201903007798), the SCOR Corporate Foundation for Science, a Strategic Positioning Fund for Genetic Orphan Diseases (SPF2012/005) and an inaugural UIBR grant from the Agency for Science, Technology and Research in Singapore to BR, and the French National Research Agency (ANR) under the "Investments for the future" (grant number ANR-10-IAHU-01) and GENMSMD (ANR-16-CE17.0005-01, to JB). MO was supported by the David Rockefeller Graduate Program, the Funai Foundation for Information Technology (FFIT), the Honjo International Scholarship Foundation (HISF), the New York Hideyo Noguchi Memorial Society (HNMS), and the Cooperative Center on Human Immunology (CCHI) at The Rockefeller University. TLV and

JR are supported by the MD-PhD program of the Imagine Institute with the support of the Bettancourt-Schueller Foundation. ALN is supported by the international PhD program of the Imagine Institute with the support of the Bettancourt-Schueller Foundation. JR was also supported by a “poste d’Accueil INSERM”.

### **Authorship contributions**

TLV, JLC and JB conceived and designed the study. TLV, JLC and JB wrote the paper. Most experiments were performed by TLV under the supervision of JB and JLC. ALN, JR, RY and MO and VB performed functional experiments. DW and PB contributed to the analysis of immunofluorescence. LB and NB contributed to the interpretation of CT-scan and MRI. MO, CG, SBD, RY and DB contributed to CyTOF and functional experiments with PBMCs. FR performed viral serological analyses, FAA, MA, TK and NM performed and analyzed phage immunoprecipitation-sequencing (VirScan). MR, MCh, SBD, SYZ, contributed new reagents/analytic tools, SB, AF, AM, DM, SAM, FAM, FA, MA, DS, ABA, BR provided samples and performed clinical diagnosis and follow-up of the kindreds. FR, BB, LA and YS contributed to WES analysis. LR DR, JB, SBD and TLV recorded the clinical data. JB, SBD and TLV created the figures. All authors commented on and discussed the paper and approved the final manuscript as submitted.



## References

1. Bustamante J (2020) Mendelian susceptibility to mycobacterial disease: recent discoveries. *Hum Genet* 139(6-7):993-1000.
2. Bustamante J, Boisson-Dupuis S, Abel L, & Casanova JL (2014) Mendelian susceptibility to mycobacterial disease: genetic, immunological, and clinical features of inborn errors of IFN-gamma immunity. *Semin Immunol* 26(6):454-470.
3. Yang R, *et al.* (2020) Human T-bet Governs Innate and Innate-like Adaptive IFN-gamma Immunity against Mycobacteria. *Cell* 183(7):1826-1847 e1831.
4. Kerner G, *et al.* (2020) Inherited human IFN-gamma deficiency underlies mycobacterial disease. *J Clin Invest* 130(6):3158-3171.
5. Nathan CF, Murray HW, Wiebe ME, & Rubin BY (1983) Identification of interferon-gamma as the lymphokine that activates human macrophage oxidative metabolism and antimicrobial activity. *J Exp Med* 158(3):670-689.
6. Bogunovic D, *et al.* (2012) Mycobacterial disease and impaired IFN-gamma immunity in humans with inherited ISG15 deficiency. *Science* 337(6102):1684-1688.
7. Kreins AY, *et al.* (2015) Human TYK2 deficiency: Mycobacterial and viral infections without hyper-IgE syndrome. *J Exp Med* 212(10):1641-1662.
8. Okada S, *et al.* (2015) IMMUNODEFICIENCIES. Impairment of immunity to *Candida* and *Mycobacterium* in humans with bi-allelic RORC mutations. *Science* 349(6248):606-613.
9. Eletto D, *et al.* (2016) Biallelic JAK1 mutations in immunodeficient patient with mycobacterial infection. *Nat Commun* 7:13992.
10. Dupuis S, *et al.* (2003) Impaired response to interferon-alpha/beta and lethal viral disease in human STAT1 deficiency. *Nat Genet* 33(3):388-391.
11. Hsu AP, *et al.* (2011) Mutations in GATA2 are associated with the autosomal dominant and sporadic monocytopenia and mycobacterial infection (MonoMAC) syndrome. *Blood* 118(10):2653-2655.
12. Dickinson RE, *et al.* (2011) Exome sequencing identifies GATA-2 mutation as the cause of dendritic cell, monocyte, B and NK lymphoid deficiency. *Blood* 118(10):2656-2658.
13. Oleaga-Quintas C, *et al.* (2021) Inherited GATA2 Deficiency Is Dominant by Haploinsufficiency and Displays Incomplete Clinical Penetrance. *J Clin Immunol*.
14. Boisson-Dupuis S, *et al.* (2015) Inherited and acquired immunodeficiencies underlying tuberculosis in childhood. *Immunol Rev* 264(1):103-120.
15. Boisson-Dupuis S, *et al.* (2018) Tuberculosis and impaired IL-23-dependent IFN-gamma immunity in humans homozygous for a common TYK2 missense variant. *Sci Immunol* 3(30).
16. Kerner G, *et al.* (2021) Human ancient DNA analyses reveal the high burden of tuberculosis in Europeans over the last 2,000 years. *Am J Hum Genet* in press.
17. Kerner G, *et al.* (2019) Homozygosity for TYK2 P1104A underlies tuberculosis in about 1% of patients in a cohort of European ancestry. *Proc Natl Acad Sci U S A* 116(21):10430-10434.
18. Tangye SG, *et al.* (2020) Human Inborn Errors of Immunity: 2019 Update on the Classification from the International Union of Immunological Societies Expert Committee. *J Clin Immunol* 40(1):24-64.
19. Boisson-Dupuis S (2020) The monogenic basis of human tuberculosis. *Hum Genet* 139(6-7):1001-1009.
20. Rapaport F, *et al.* (2021) Negative selection on human genes underlying inborn errors depends on disease outcome and both the mode and mechanism of inheritance. *Proc Natl Acad Sci U S A* 118(3).

21. Scott EM, *et al.* (2016) Characterization of Greater Middle Eastern genetic variation for enhanced disease gene discovery. *Nat Genet* 48(9):1071-1076.
22. Itan Y, *et al.* (2016) The mutation significance cutoff: gene-level thresholds for variant predictions. *Nat Methods* 13(2):109-110.
23. Fairman-Williams ME, Guenther UP, & Jankowsky E (2010) SF1 and SF2 helicases: family matters. *Curr Opin Struct Biol* 20(3):313-324.
24. Ishidate T, *et al.* (2018) ZNFX-1 Functions within Perinuclear Nuage to Balance Epigenetic Signals. *Mol Cell* 70(4):639-649 e636.
25. Wan G, *et al.* (2018) Spatiotemporal regulation of liquid-like condensates in epigenetic inheritance. *Nature* 557(7707):679-683.
26. Wang Y, *et al.* (2019) Mitochondria-localised ZNFX1 functions as a dsRNA sensor to initiate antiviral responses through MAVS. *Nat Cell Biol* 21(11):1346-1356.
27. Itan Y, *et al.* (2015) The human gene damage index as a gene-level approach to prioritizing exome variants. *Proc Natl Acad Sci U S A* 112(44):13615-13620.
28. Petrovski S, *et al.* (2015) The Intolerance of Regulatory Sequence to Genetic Variation Predicts Gene Dosage Sensitivity. *PLoS Genet* 11(9):e1005492.
29. Kim MS, *et al.* (2014) A draft map of the human proteome. *Nature* 509(7502):575-581.
30. Satori CP, *et al.* (2013) Bioanalysis of eukaryotic organelles. *Chem Rev* 113(4):2733-2811.
31. Font J & Mackay JP (2010) Beyond DNA: zinc finger domains as RNA-binding modules. *Methods Mol Biol* 649:479-491.
32. Mazroui R, *et al.* (2002) Trapping of messenger RNA by Fragile X Mental Retardation protein into cytoplasmic granules induces translation repression. *Hum Mol Genet* 11(24):3007-3017.
33. Tourriere H, *et al.* (2003) The RasGAP-associated endoribonuclease G3BP assembles stress granules. *J Cell Biol* 160(6):823-831.
34. Gilks N, *et al.* (2004) Stress granule assembly is mediated by prion-like aggregation of TIA-1. *Mol Biol Cell* 15(12):5383-5398.
35. Wilczynska A, Aigueperse C, Kress M, Dautry F, & Weil D (2005) The translational regulator CPEB1 provides a link between dcp1 bodies and stress granules. *J Cell Sci* 118(Pt 5):981-992.
36. Somasekharan SP, *et al.* (2020) G3BP1-linked mRNA partitioning supports selective protein synthesis in response to oxidative stress. *Nucleic Acids Res* 48(12):6855-6873.
37. Hubstenberger A, *et al.* (2017) P-Body Purification Reveals the Condensation of Repressed mRNA Regulons. *Mol Cell* 68(1):144-157 e145.
38. Devos R, *et al.* (1982) Molecular cloning of human immune interferon cDNA and its expression in eukaryotic cells. *Nucleic Acids Res* 10(8):2487-2501.
39. Gray PW & Goeddel DV (1982) Structure of the human immune interferon gene. *Nature* 298(5877):859-863.
40. Martinez-Barricarte R, *et al.* (2018) Human IFN-gamma immunity to mycobacteria is governed by both IL-12 and IL-23. *Sci Immunol* 3(30).
41. Takata K, *et al.* (2017) Induced-Pluripotent-Stem-Cell-Derived Primitive Macrophages Provide a Platform for Modeling Tissue-Resident Macrophage Differentiation and Function. *Immunity* 47(1):183-198 e186.
42. Rosain J, *et al.* (2019) Mendelian susceptibility to mycobacterial disease: 2014-2018 update. *Immunol Cell Biol* 97(4):360-367.
43. Hambleton S, *et al.* (2011) IRF8 mutations and human dendritic-cell immunodeficiency. *N Engl J Med* 365(2):127-138.

44. Kong XF, *et al.* (2018) Disruption of an antimycobacterial circuit between dendritic and helper T cells in human SPPL2a deficiency. *Nat Immunol* 19(9):973-985.
45. Bigley V, Cytlak U, & Collin M (2019) Human dendritic cell immunodeficiencies. *Semin Cell Dev Biol* 86:50-61.
46. Collin M, Dickinson R, & Bigley V (2015) Haematopoietic and immune defects associated with GATA2 mutation. *Br J Haematol* 169(2):173-187.
47. Shi C & Pamer EG (2011) Monocyte recruitment during infection and inflammation. *Nat Rev Immunol* 11(11):762-774.
48. Dutta P & Nahrendorf M (2014) Regulation and consequences of monocytosis. *Immunol Rev* 262(1):167-178.
49. Calvo KR, *et al.* (2015) JMML and RALD (Ras-associated autoimmune leukoproliferative disorder): common genetic etiology yet clinically distinct entities. *Blood* 125(18):2753-2758.
50. Niemeyer CM & Flotho C (2019) Juvenile myelomonocytic leukemia: who's the driver at the wheel? *Blood* 133(10):1060-1070.
51. Hasle H (2016) Myelodysplastic and myeloproliferative disorders of childhood. *Hematology Am Soc Hematol Educ Program* 2016(1):598-604.
52. Donadieu J, *et al.* (2018) Natural history of GATA2 deficiency in a survey of 79 French and Belgian patients. *Haematologica* 103(8):1278-1287.
53. Lachmann N, *et al.* (2015) Large-scale hematopoietic differentiation of human induced pluripotent stem cells provides granulocytes or macrophages for cell replacement therapies. *Stem Cell Reports* 4(2):282-296.
54. Abdel-Nour M, *et al.* (2019) The heme-regulated inhibitor is a cytosolic sensor of protein misfolding that controls innate immune signaling. *Science* 365(6448).
55. Gomes E & Shorter J (2019) The molecular language of membraneless organelles. *J Biol Chem* 294(18):7115-7127.
56. Kedersha N, *et al.* (2005) Stress granules and processing bodies are dynamically linked sites of mRNP remodeling. *J Cell Biol* 169(6):871-884.
57. Anderson P & Kedersha N (2009) Stress granules. *Curr Biol* 19(10):R397-398.
58. Burgess HM & Mohr I (2018) Defining the Role of Stress Granules in Innate Immune Suppression by the Herpes Simplex Virus 1 Endoribonuclease VHS. *J Virol* 92(15).
59. McCormick C & Khapersky DA (2017) Translation inhibition and stress granules in the antiviral immune response. *Nat Rev Immunol* 17(10):647-660.
60. Li H & Durbin R (2009) Fast and accurate short read alignment with Burrows-Wheeler transform. *Bioinformatics* 25(14):1754-1760.
61. McKenna A, *et al.* (2010) The Genome Analysis Toolkit: a MapReduce framework for analyzing next-generation DNA sequencing data. *Genome Res* 20(9):1297-1303.
62. Li H, *et al.* (2009) The Sequence Alignment/Map format and SAMtools. *Bioinformatics* 25(16):2078-2079.
63. Esteve-Sole A, *et al.* (2018) Laboratory evaluation of the IFN-gamma circuit for the molecular diagnosis of Mendelian susceptibility to mycobacterial disease. *Crit Rev Clin Lab Sci* 55(3):184-204.
64. Feinberg J, *et al.* (2004) Bacillus Calmette Guerin triggers the IL-12/IFN-gamma axis by an IRAK-4- and NEMO-dependent, non-cognate interaction between monocytes, NK, and T lymphocytes. *Eur J Immunol* 34(11):3276-3284.
65. Ogishi M, *et al.* (2021) Multibatch Cytometry Data Integration for Optimal Immunophenotyping. *J Immunol* 206(1):206-213.
66. Korsunsky I, *et al.* (2019) Fast, sensitive and accurate integration of single-cell data with Harmony. *Nat Methods* 16(12):1289-1296.

67. Van Gassen S, *et al.* (2015) FlowSOM: Using self-organizing maps for visualization and interpretation of cytometry data. *Cytometry A* 87(7):636-645.
68. Wilkerson MD & Hayes DN (2010) ConsensusClusterPlus: a class discovery tool with confidence assessments and item tracking. *Bioinformatics* 26(12):1572-1573.
69. Meuwis MA, *et al.* (2007) Biomarker discovery for inflammatory bowel disease, using proteomic serum profiling. *Biochem Pharmacol* 73(9):1422-1433.

## Figure Legends

**Figure 1: Autosomal recessive ZNFX1 deficiency in four patients from two unrelated kindreds.** **A.** Pedigrees of the two unrelated kindreds. Generations are indicated by Roman numerals (I-II) and each individual is indicated by an Arabic numeral (1-7). Affected patients are represented by closed black symbols and index cases are indicated by an arrow. “E?” indicates individuals with an unknown genotype. Symbols crossed with a black diagonal line correspond to deceased individuals. **B.** Schematic representation of the *ZNFX1* gene. Coding exons are indicated by Roman numerals (II to XIV). The ZNFX1 protein is represented, with three predicted domains: the Armadillo (ARM), helicase and zinc-finger (ZNF) domains. The reported mutations are indicated in red with an arrow. **C.** Principal component analysis (PCA) showing the origins of P1, P2 and P3 plotted on main ethnic origins extracted from the 1000 Genomes database and our own WES database. **D.** Minor allele frequency (MAF) and combined annotation-dependent depletion (CADD) score of the homozygous *ZNFX1* variants found in P1-P3 (red symbols) and of all homozygous variants in gnomAD v.2.1.1 and BRAVO/TOP2 (black symbols). The dotted line corresponds to the mutation significance cutoff (MSC), with its 99% confidence interval. The MSC for *ZNFX1* is 3.3. **E.** According to its residual variation intolerance score (RVIS), *ZNFX1* is highly intolerant of genetic variation. **F.** Consensus negative selection score (CoNeS) for *ZNFX1* and its distribution for genes causing inborn errors of immunity (IEI), according to disease mode of inheritance (AD: autosomal dominant, AR: autosomal recessive). **G.** RT-qPCR on cDNA from HEK293T cells non-transfected (NT) or transfected with an empty plasmid (EV), wild-type (WT)-*ZNFX1*, mutated-*ZNFX1* (E1606Rfs\*10 and S959\*) or constructs with in-frame deletions of each ZNFX1 domain, for the ARM (c.30\_2028del), helicase (c.2094\_3780del) and ZNF (c.3801\_5503del) domains, with a probe spanning the junction between exons 3-4 (probe 1, left panel) or exons 13 and 14 (probe 2, right panel). *GUSB* was used for normalization. Values are expressed as

means  $\pm$  SEM. **H.** Western blot of total protein extracts from HEK293T cells either left NT or transfected with EV, WT or mutated *ZNFX1*, or constructs with in-frame deletions of the ARM (c.30\_2028del), helicase (c.2094\_3780del) or ZNF (c.3801\_5503del) domain, all inserted into pCMV6 with a C-terminal Flag-tag. *ZNFX1* was detected with a monoclonal antibody directed against the N-terminus of *ZNFX1* or an antibody directed against the C-terminal DDK (Flag)-tag. An antibody against vinculin was used as a loading control. The results shown are representative of two independent experiments.

**Figure 2. Expression of ZNFX1 in cell lines from patients.** **A.** Confocal microscopy of HeLa cells transiently transfected with an empty vector (EV) or the WT-*ZNFX1*, stained with the anti-G3BP1 antibody, DAPI or an antibody directed against the C-terminus of *ZNFX1*. The scale bar represents 10  $\mu$ m. **B.** Colocalization of *ZNFX1* and G3BP1 in SV40 fibroblasts stimulated 24h with 25  $\mu$ g/mL of poly(I:C) from a healthy control and a *ZNFX1* deficient patient (P2), treated or not with 0.5 mM arsenite for 30 minutes. **C.** Colocalization of *ZNFX1* and G3BP1 in adherent THP1 cells treated or not with 0.5 mM arsenite for 30 minutes. An IgG isotype is used as a negative control. The results shown are representative of at least two independent experiments. Scale bar represents 10  $\mu$ m. **D.** RT-qPCR for *ZNFX1* with a probe spanning the junction between exons 3 and 4 (left) or spanning the junction between exons 13 and 14 (right) in EBV-B cells from healthy controls ( $n=3$ ) and a patient (P1). *GUSB* was used for normalization. Values are expressed as means  $\pm$  SEM. **E.** RT-qPCR for *ZNFX1* with a probe spanning the junction between exons 13 and 14 (left) and a probe spanning the junction between exons 3 and 4 (right) in SV40 fibroblasts from healthy controls ( $n=3$ ) and patients (P1 and P2). *GUSB* was used for normalization. Values are expressed as means  $\pm$  SEM. **F.** Western blot of total protein extracts from EBV-B cells from healthy controls (C1, C2) and a patient (P1). *ZNFX1* was detected with

a monoclonal antibody directed against the N-terminus. An antibody against tubulin was used as a loading control. The results shown are representative of two independent experiments. **E.** Western blot of total protein extracts from SV40 fibroblasts from healthy controls (C1, C2 and C3) and patients (P1 and P2). ZNFX1 was detected with a monoclonal antibody directed against the N-terminus. An antibody against tubulin was used as a loading control. The results shown are representative of two independent experiments.

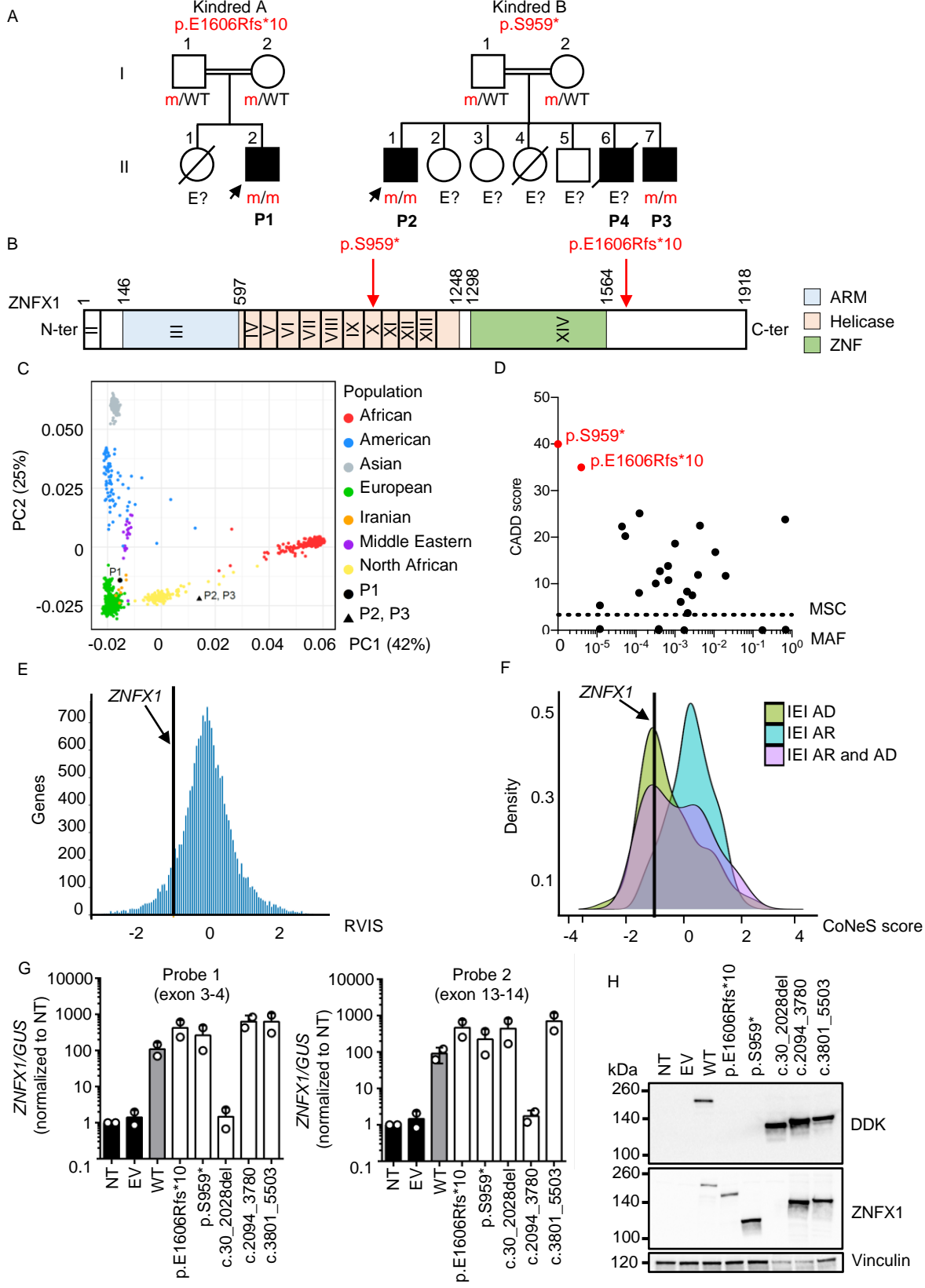
**Figure 3: Hematological and immunological profile of patients with inherited ZNFX1 deficiency.** **A.** Absolute numbers of peripheral total leukocytes, neutrophils, lymphocytes, monocytes, hemoglobin and platelets from P1, P2 and P3, determined from complete blood counts. **B.** UMAP analysis of CyTOF showing the distribution of the main peripheral leukocyte populations identified in a healthy control, P1, P2 and P3. **C.** Frequency of living CD4<sup>+</sup> T cells and their subsets in adult controls (green circles), age-matched controls (blue circles) and P1, P2, P3 (red circles), as determined by CyTOF. **D.** Frequency of living CD8<sup>+</sup> T cells and their subsets, **E.** B cells, **F.**  $\gamma\delta$  T cells, **G.** NK cells and their subsets, **H.** MAIT cells, **I.** Frequency of monocytes and their subsets **J.** Eosinophils, **K.** Basophils, and **L.** Dendritic cells (DCs) and their subsets, as determined by CyTOF. Results are expressed as a proportion of living single peripheral blood mononuclear cells (PBMCs).

**Figure 4: Conserved IFN- $\gamma$  immunity in ZNFX1-deficient patients.** PBMCs from controls (green dots), age-matched controls (blue dots) and patients with AR ZNFX1 deficiency (red dots) were left unstimulated or were stimulated with IL-12, or IL-23, with or without BCG activation. **A.** IFN- $\gamma$  levels in the supernatant of PBMCs with and without stimulation with IL-12, IL-23, BCG, BCG+IL-12 and BCG+IL-23, as assessed by intracellular flow cytometry. Proportion of IFN- $\gamma$ -producing lymphocytes of various subsets involved in innate (NK, iNKT

and MAIT cells), adaptive ( $CD4^+$  and  $CD8^+$  T cells) and both adaptive and innate ( $\gamma\delta$  T cells including  $V\delta 1^+$ ,  $V\delta 2^+$  and  $V\delta 1^-V\delta 2^-$  subsets) immunity after stimulation with **B.** BCG, **C.** IL-12, **D.** BCG+ IL-12, **E.** IL-23, or **F.** BCG+IL-23. **G.** Secretion of IL-12p40 by whole blood from daily controls ( $n=69$ ), travel controls ( $n=14$ ), P1, with and without stimulation with BCG alone, or BCG and IFN- $\gamma$ . ELISA was used to determine the levels of this cytokine. **H.** Secretion of IL-12 p40 by EBV-B cells from controls, patients with AR complete IL-12p40 deficiency (IL-12p40 $^{-/-}$ ) or P1, after stimulation with  $10^{-7}$  M PDBu for 24 hours. ELISA was used to determine the levels of these cytokines. **I.** Phosphorylation of STAT1 after 20 minutes of stimulation with IFN- $\gamma$  ( $10^4$  IU/mL) or IFN- $\alpha$  ( $10^4$  IU/mL) in EBV-B cells from a healthy control (C+), P1 and a patient with AR complete STAT1 deficiency (STAT1 $^{-/-}$ ), as determined by flow cytometry. **J.** Induction of HLA-DR expression in SV40 fibroblasts from controls (C+), P1, P2, and a patient with AR complete IFN- $\gamma$ R1 deficiency (IFN- $\gamma$ R1 $^{-/-}$ ) after 48 h of stimulation with IFN- $\gamma$  ( $10^4$  IU/mL), as determined by flow cytometry. The results of **I** and **J** are representative of two independent experiments.



Figure 1



Supplementary Figure 1

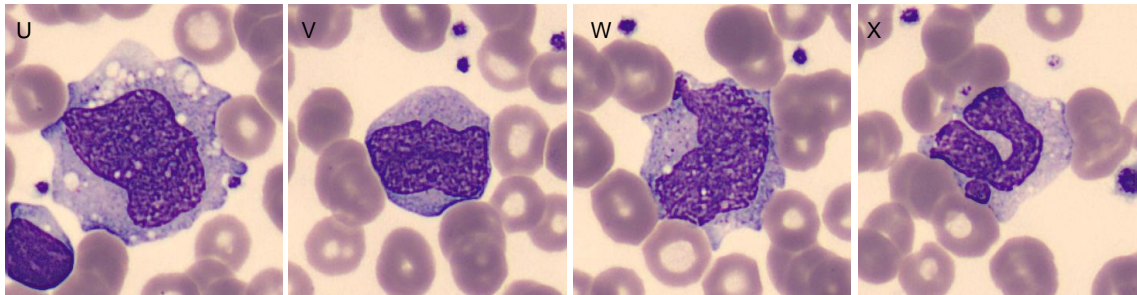
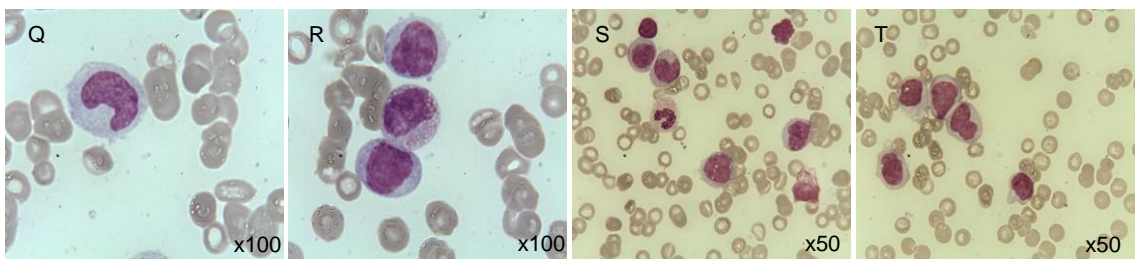
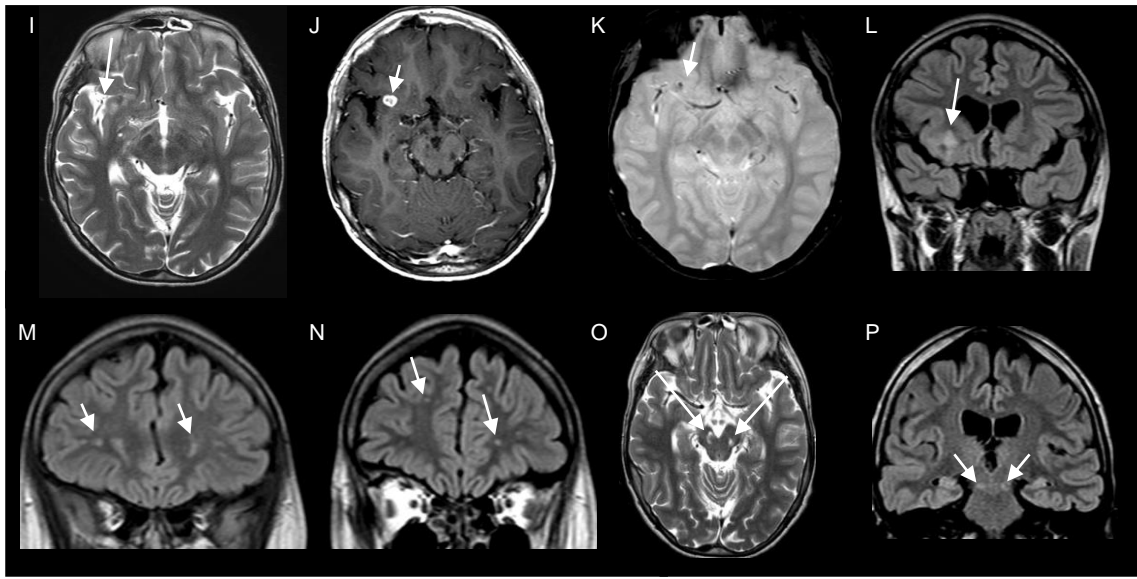
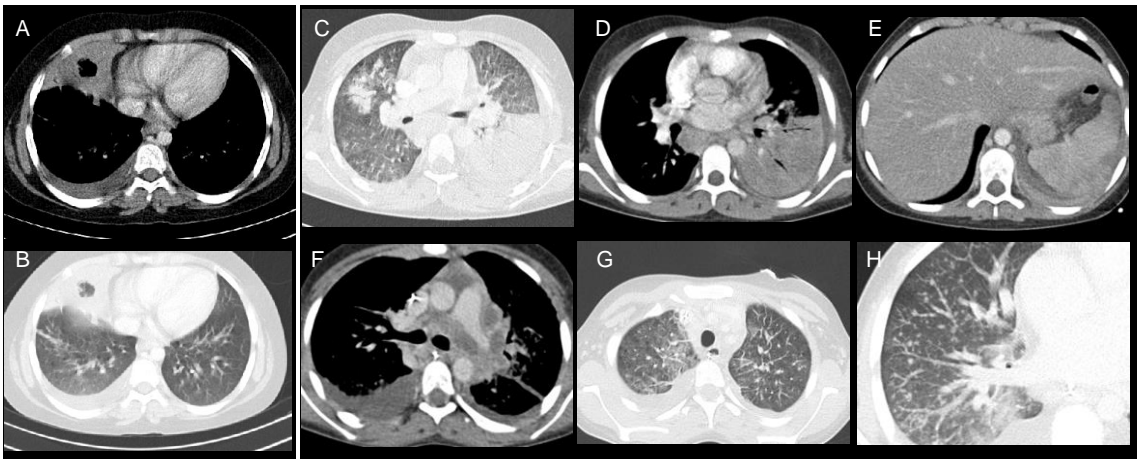
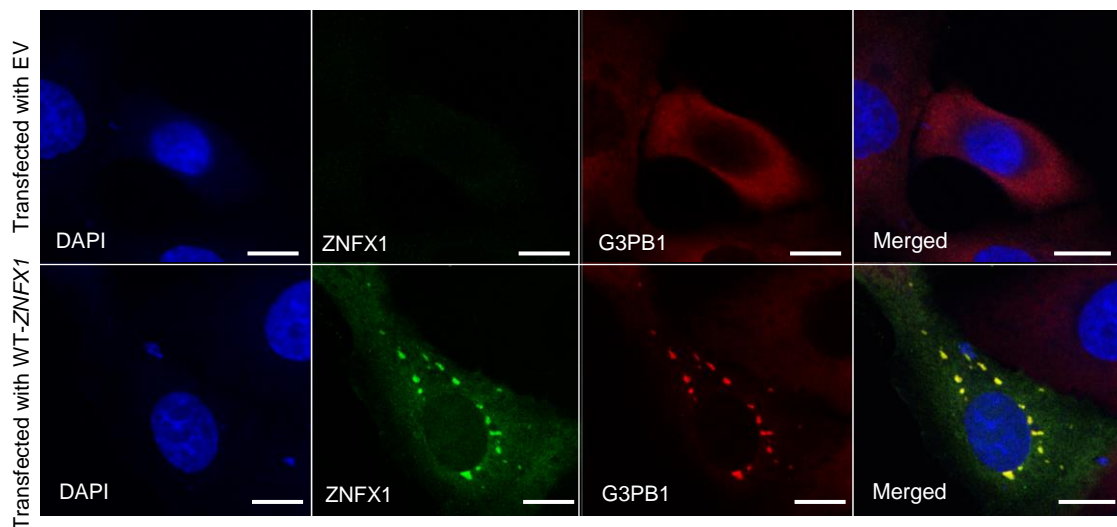
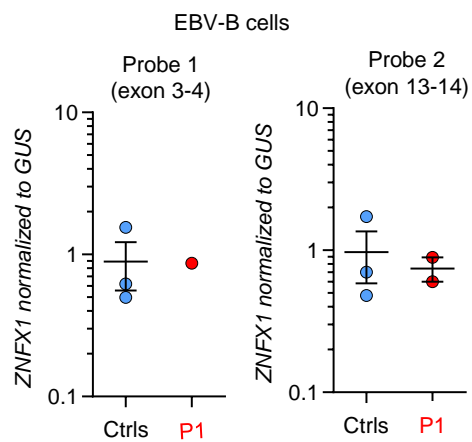


Figure 2

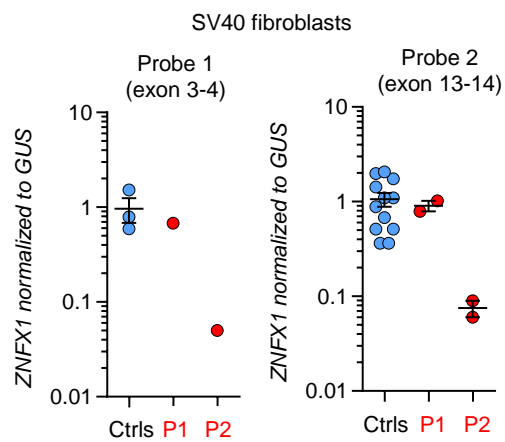
A



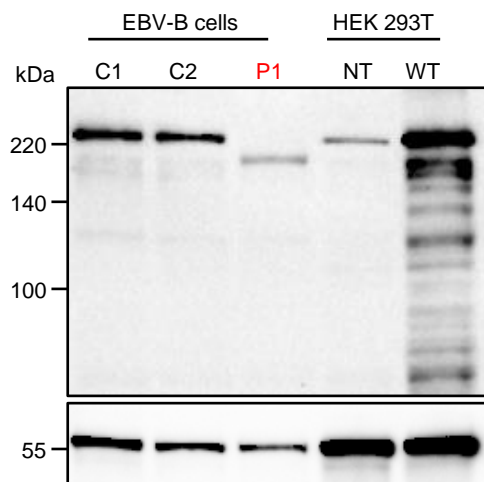
B



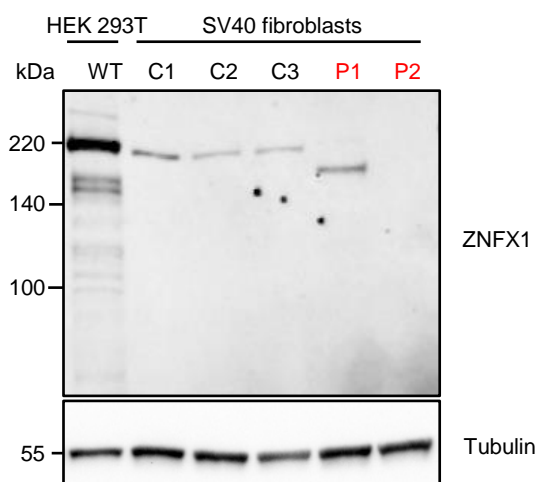
C



D

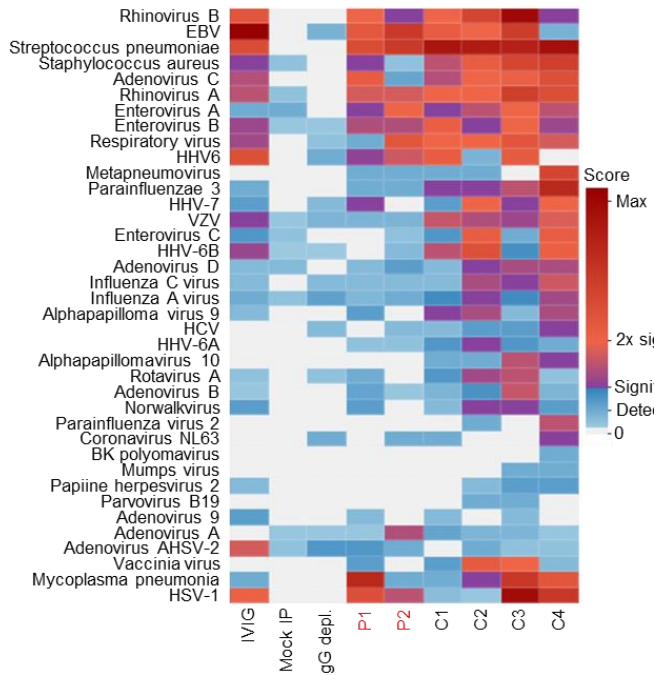


E

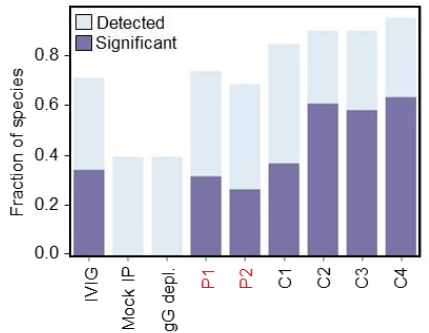


Supplementary Figure 2

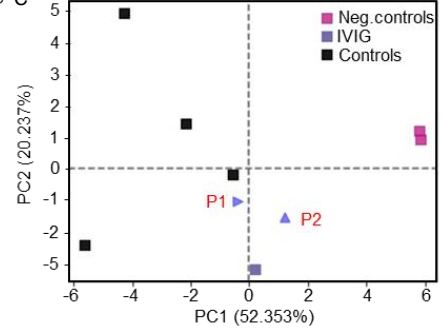
A



B



C



Supplementary Figure 3

**A**

	P1	P2	P3
Homozygosity rate	4.9%	2.2%	1.7%
Variants	130,401	159,860	136,523
Rare variant (<1%) within coding and essential splicing site	635	770	974
CADD > MSC Blacklist: no GDI <13	418	479	557
Homozygous predicted deleterious variants	34	30	42
Shared homozygous variants between P1, P2 and P3	1 gene (ZNF1)		

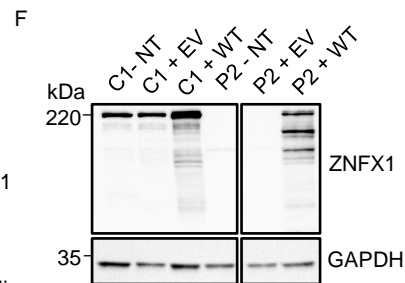
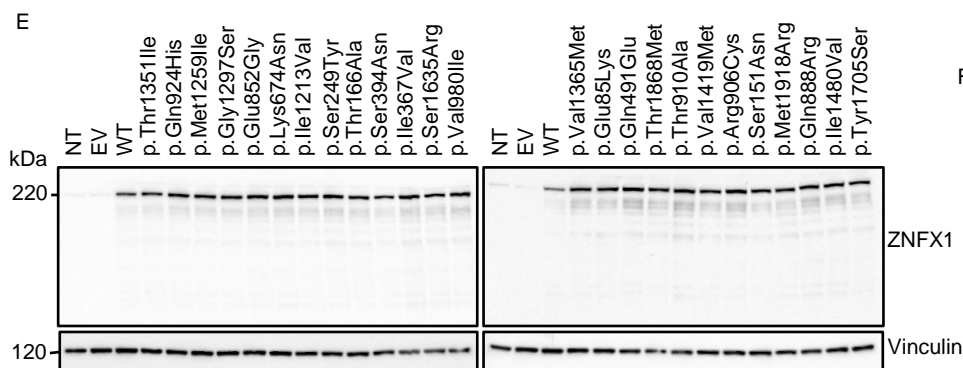
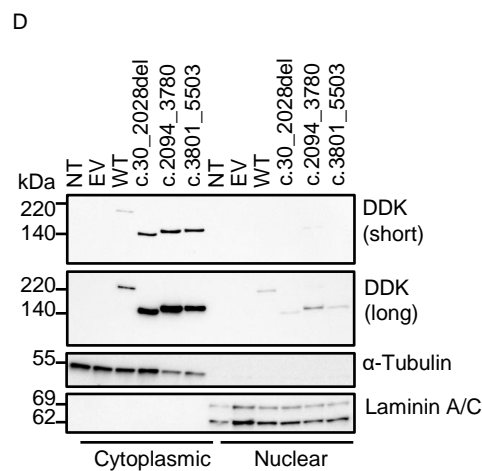
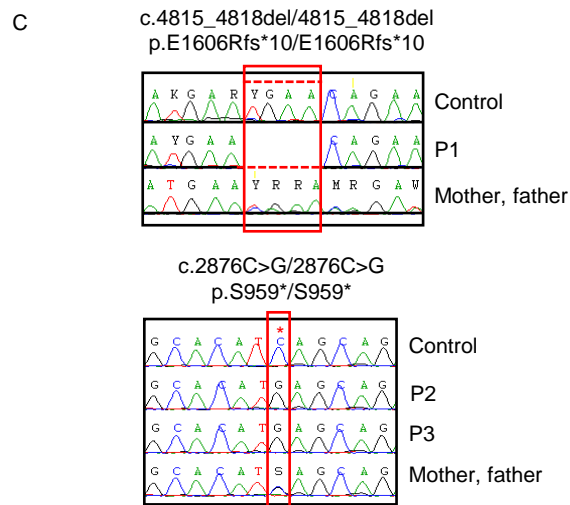
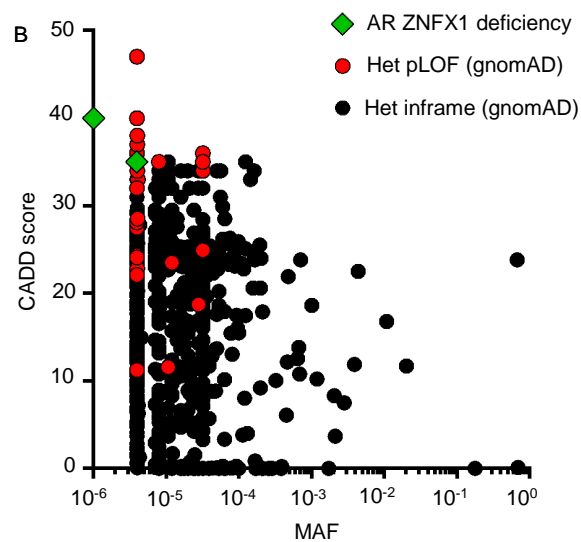
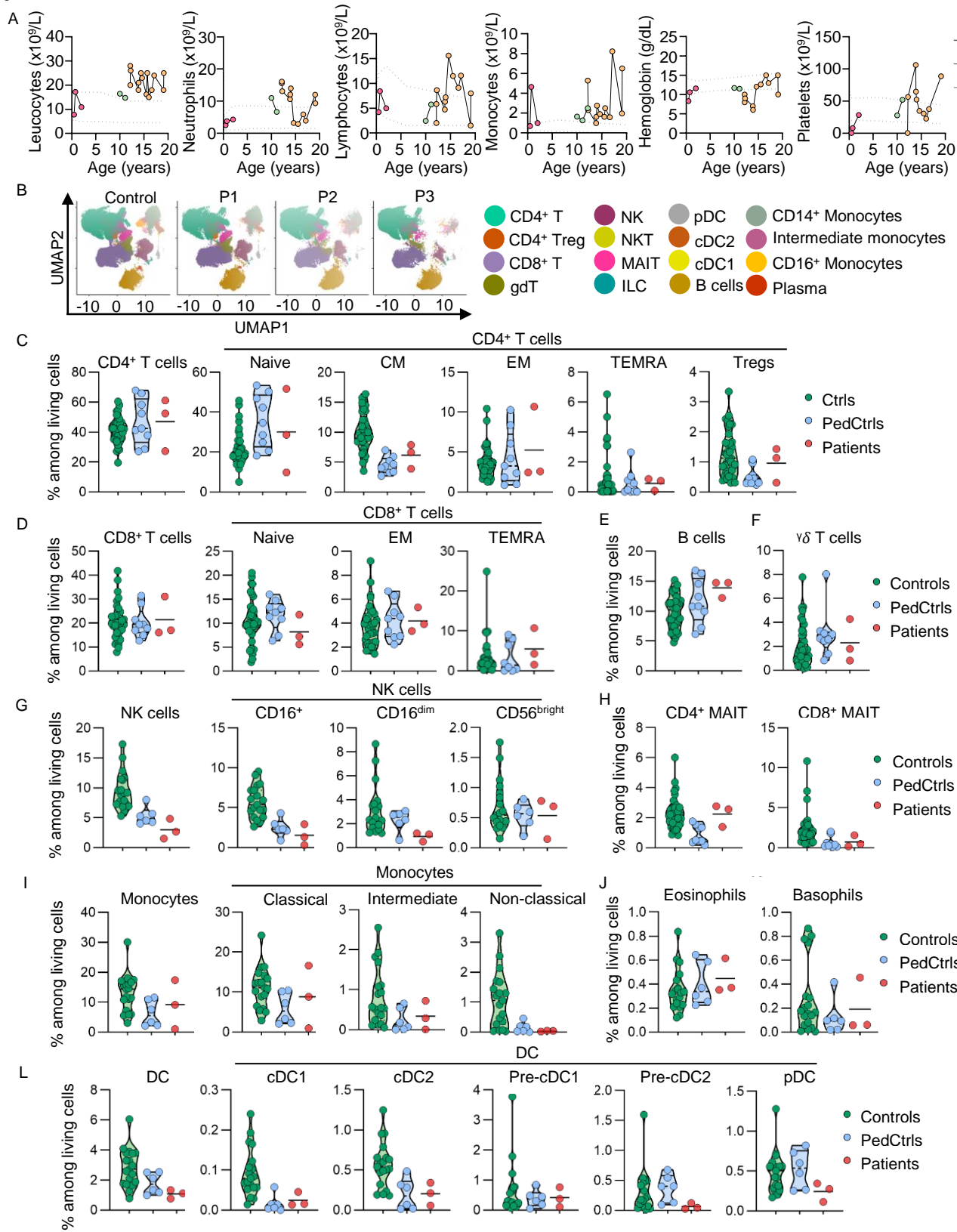
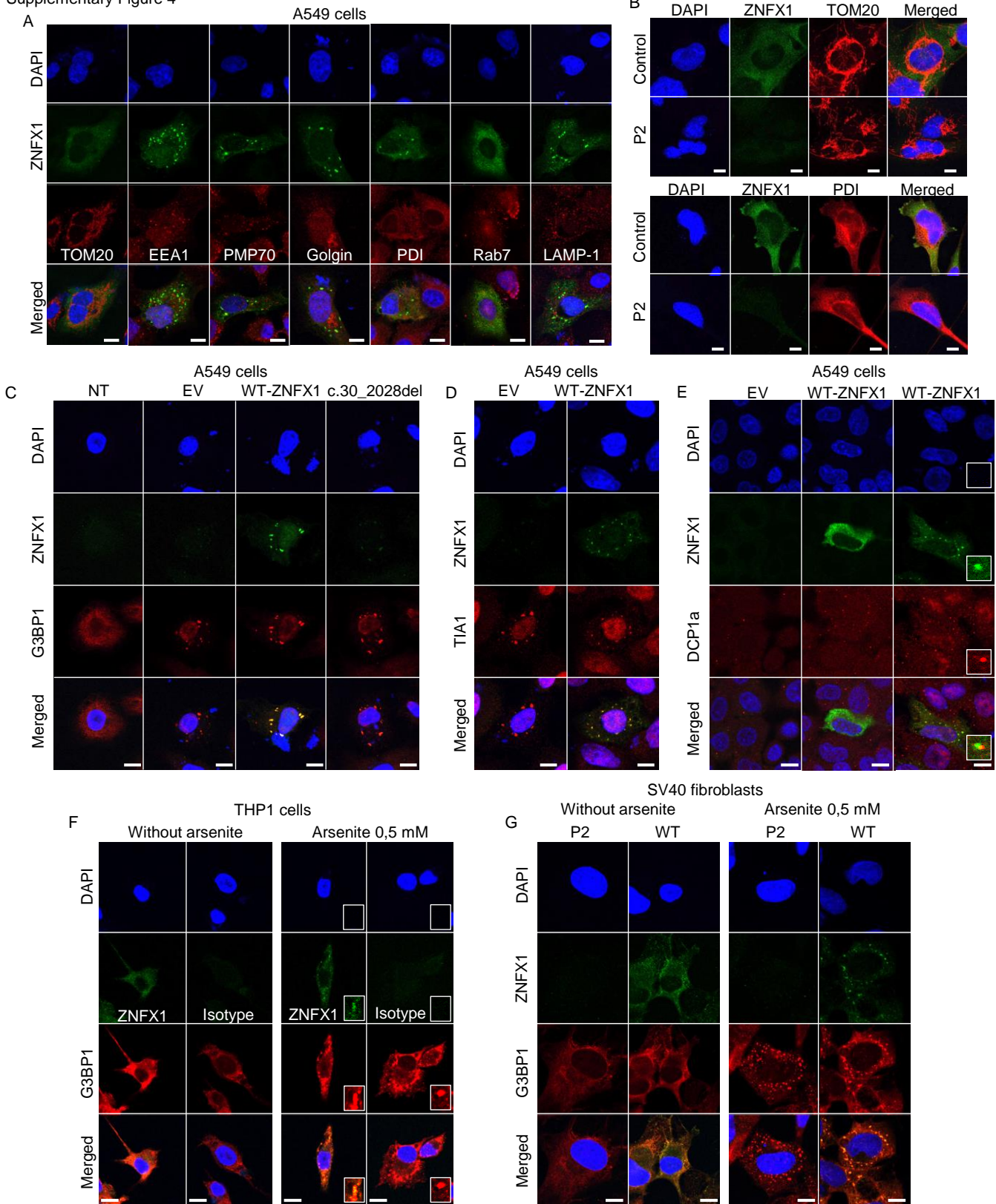
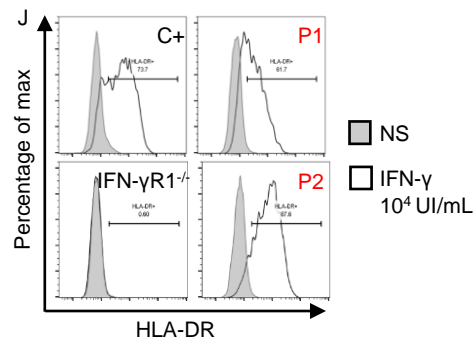
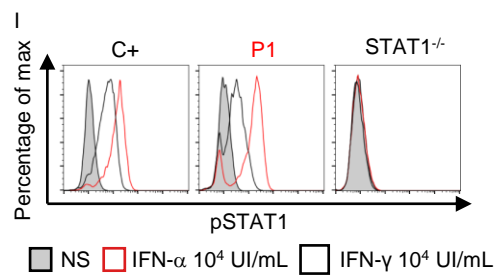
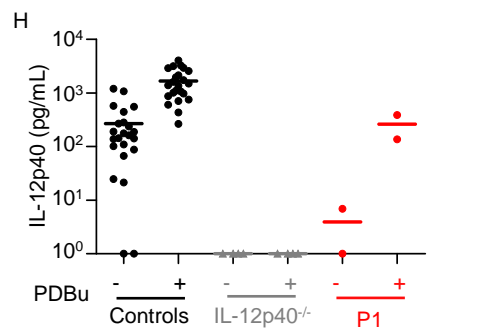
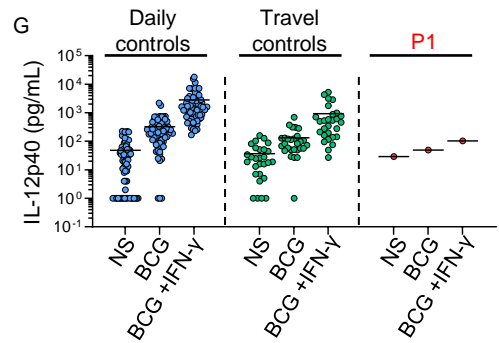
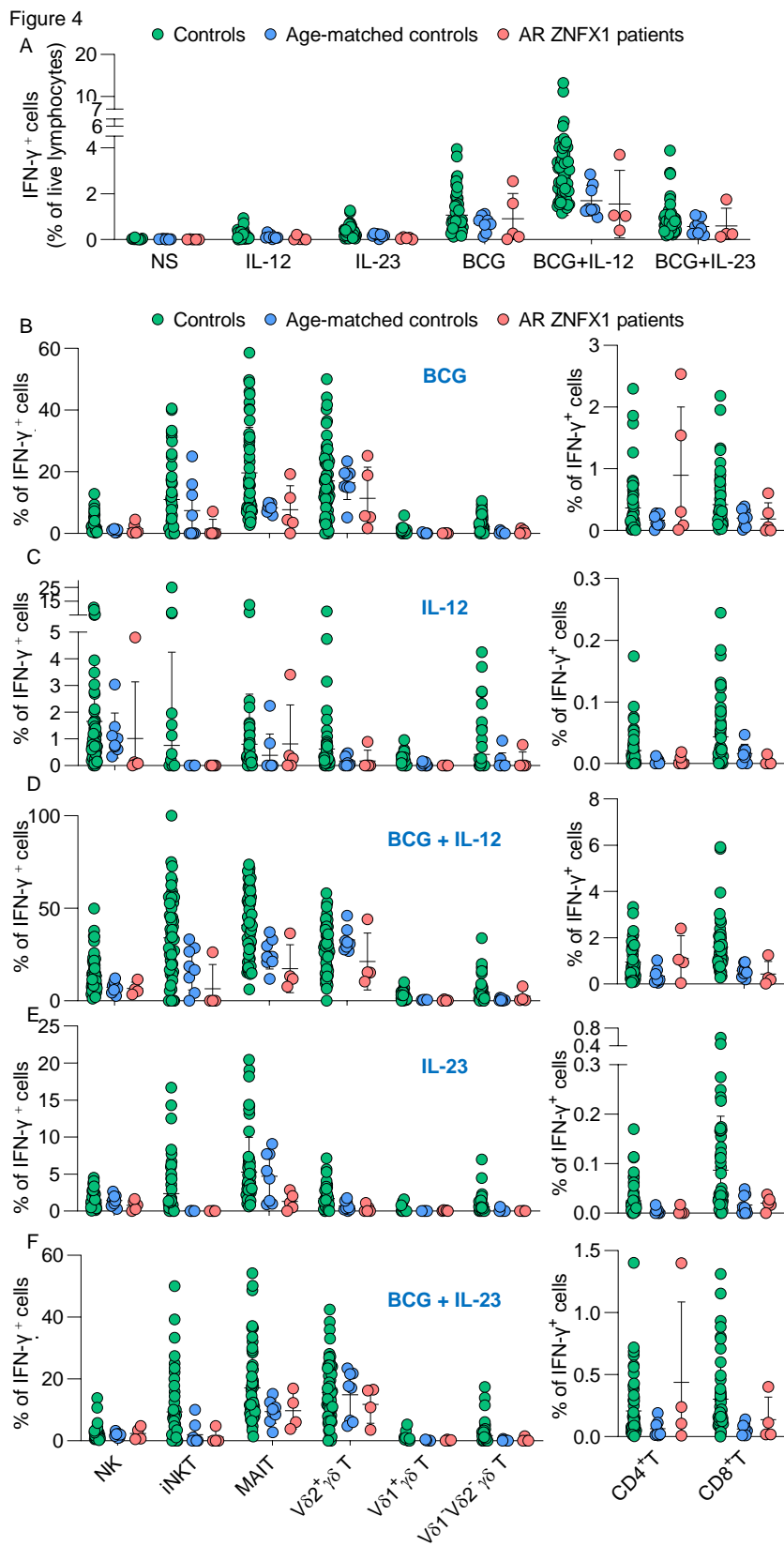


Figure 3



Supplementary Figure 4







Supplementary Figure 5

